A fast Fourier transform-based mesoscale field dislocation mechanics study of grain size effects and reversible plasticity in polycrystals

Stéphane Berbenni, Vincent Taupin, Ricardo A Lebensohn

A fast Fourier transform-based mesoscale field dislocation mechanics study of grain size effects and reversible plasticity in polycrystals

Stéphane Berbenni [a,c,1], Vincent Taupin [a,c],

Ricardo A. Lebensohn [b]

[a] *Université de Lorraine, Arts et Métiers Paris Tech, CNRS, LEM3, F-57000 Metz, France*

[b] *Theoretical Division, Los Alamos National Laboratory, Los Alamos, NM 87845, USA*

[c] *Laboratory of Excellence on Design of Alloy Metals for low-mAss Structures (DAMAS), Université de Lorraine, France*

Abstract

A numerical implementation of a non-local polycrystal plasticity theory based on a mesoscale version of the field dislocation mechanics theory (MFDM) of Acharya and Roy (2006) is presented using small-strain elasto-viscoplastic fast Fourier transform-based (EVPFFT) algorithm developed by Lebensohn et al. (2012). In addition to considering plastic flow and hardening only due to SSDs (statistically stored dislocations) as in the classic EVPFFT framework, the proposed method accounts for the evolution of GND (geometrically necessary dislocations) densities solving a hyperbolic-type partial differential equation, and GND effects on both plastic flow and hardening. This allows consideration of an enhanced strain-hardening law that

includes the effect of the GND density tensor. The numerical implementation of a reduced version of the MFDM is presented in the framework of the FFT-based augmented Lagrangian procedure of Michel et al. (2001). A Finite Differences scheme combined with discrete Fourier transforms is applied to solve both incompatibility and equilibrium equations. The numerical procedure named MFDM-EVPFFT is used to perform full field simulations of polycrystal plasticity considering different grain sizes and their mechanical responses during monotonic tensile and reversible tension-compression tests. Using Voronoi tessellation and periodic boundary conditions, voxelized representative volume elements (RVEs) with different grain sizes are generated. With MFDM-EVPFFT, a Hall-Petch type scaling law is obtained in contrast with the conventional crystal plasticity EVPFFT. In the case of reversible plasticity, a stronger Bauschinger effect is observed with the MFDM-EVPFFT approach in comparison with conventional EVPFFT. The origin of these differences is analyzed in terms of heterogeneity, GND density and stress evolutions during the compression stage.

Keywords: Field dislocation mechanics; elastoviscoplastic; FFT; polycrystal; grain size effects

1 Introduction

The response of polycrystalline metals to mechanical loading is notably dependent on grain size, which is in turn dictated by thermo-mechanical processing (Hall, 1951; Petch, 1953; Armstrong et al., 1962; Meyers and Chawla, 1984; Hansen, 1985, 2004). The microstructure of metallic polycrystals induces additional hardening compared

[1] Corresponding author. This paper is dedicated to the memory of Professor Marcel Berveiller deceased on Jan 1., 2019.

Email address: stephane.berbenni@univ-lorraine.fr (Stéphane Berbenni)

with single crystals due to the presence of grain boundaries (Hirth, 1972; Thompson et al., 1973; Mecking, 1981). In polycrystals, different effects need to be considered in a crystal plasticity formulation to predict the polycrystal's behavior (Hirth, 1972; Berveiller, 1978). First of all, plastic incompatibilities inducing long range internal stresses (at the scale of the mean grain diameter) as well as inter-granular accommodation due to multiple slip in grains with different crystallographic orientations should be considered. Such effects can be accounted for using mean-field approaches like the elasto-plastic (EPSC) (Kröner, 1961; Budiansky and Wu, 1962; Hill, 1965; Berveiller and Zaoui, 1979; Masson et al., 2000), visco-plastic (VPSC) (Molinari et al., 1987; Lebensohn and Tomé, 1993) or elasto-viscoplastic (EVPSC) (Sabar et al., 2002; Mercier and Molinari, 2009; Wang et al., 2010; Mareau and Berbenni, 2015) self-consistent schemes. However, consideration of the effect of grain size is difficult in the context of such approaches. Different refined micromechanical mean field models have been proposed to extend such self-consistent schemes, by considering intra-granular back-stresses with associated internal length scales related to dislocation loops or slip bands constrained at grain boundaries (Berbenni et al., 2008; Richeton et al., 2009; Collard et al., 2010) or due to GND densities (Ashby, 1970), see e.g. Pipard et al. (2009) and Taupin et al. (2010). Moreover, the effect of neighboring grains, grain and grain boundary shapes and the presence of triple junctions, all inducing non uniform intra-granular mechanical fields also need to be accounted for. This can be achieved using full field CP-FEM (Mika and Dawson, 1998; Delaire et al., 2000; Barbe et al., 2001b,a) or EVPFFT (Lebensohn et al., 2012; Suquet et al., 2012). However, such formulations are based on conventional continuum crystal plasticity. Therefore, even though these methods are able to consider plastic anisotropy owing to the grain's crystallographic orientations and shapes, they do not account for internal length scale effects or non local effects due to slip gradients and dislocation pileups at grain boundaries. As a consequence, their main

shortcoming is that the predicted microscopic and macroscopic field responses are grain size independent.

A simple way of introducing size effects is to consider an explicit grain size dependence in the constitutive equation at the level of grains or slip systems (Weng, 1983). This method revealed to be efficient for considering grain size distribution effects on the macroscopic flow stress of polycrystals (Berbenni et al., 2007; Lavergne et al., 2013) but the size effect does not come from deformation gradients that exist at more local scale reflecting the inhomogeneous nature of slip in the presence of grain boundaries. These intra-granular spatial gradients of lattice orientation, e.g. lattice curvatures, can be measured with Electron Back-Scatterred Diffraction (EBSD) (Randle et al., 1996; Scheriau and Pippan, 2008; Beausir et al., 2009; Perrin et al., 2010). Using the relationship between lattice curvature and the GND density tensor (also called Nye tensor) given by Nye (1953) and later by Kröner (1958) or Kröner (1981), GND densities in polycrystalline metals are nowadays commonly measured using white beam micro-diffraction (Barabash et al., 2005) or using scanning electron microscopy equipped with two- or three-dimensional EBSD set up (Pantleon, 2008; Calcagnotto et al., 2010; Allain-Bonasso et al., 2012; Konijnenberg et al., 2015; Jiang et al., 2015; Wallis et al., 2016).

Alternatively, Discrete Dislocation Dynamics (DDD) methods first developed by Kubin et al. (1992) and later by Van der Giessen and Needleman (1995), Verdier et al. (1998), Schwarz (1999) among others, are able to naturally account for internal length and grain size effects considering discrete distributions of dislocation sources, dislocation mobility, Peach-Koehler force (Peach and Koehler, 1950) on dislocation line or segments and impenetrable grain or phase boundaries. For example, DDD was used to study plasticity size effects on internal stresses in thin films (Espinosa et al., 2005, 2006), micro-specimens (Kiener et al., 2010), grain size effects on the

strengthening of polycrystals and Hall-Petch relationship (Biner and Morris, 2002; Lefebvre et al., 2007; Balint et al., 2010; Jiang et al., 2019) and Bauschinger effect (Nicola et al., 2006; Guruprasad et al., 2008; Balint et al., 2010; Jiang et al., 2019; Waheed et al., 2017).

On the other hand, strain gradient plasticity continuum theories (Fleck and Hutchinson, 1993; Smyshlyaev and Fleck, 1996; Fleck and Hutchinson, 2001; Niordson and Hutchinson, 2003; Gudmundson, 2004; Zeghadi et al., 2005; Gurtin and Anand, 2009; Niordson and Legarth, 2010; Fleck and Willis, 2009; Fleck et al., 2015; El-Naaman et al., 2019) are also able to predict size dependent responses of polycrystals like Hall-Petch behavior and reversible plasticity effects due to GNDs. These theories integrate the Nye tensor characterizing the plastic deformation incompatibility and strain gradient effects in continuum crystal plasticity simulations. Strain gradient plasticity theories were also coupled with crystal plasticity framework with both SSDs and GNDs (Arsenlis and Parks, 1999, 2002; Acharya and Bassani, 2000; Acharya and Beaudoin, 2000; Evers et al., 2002, 2004; Gurtin et al., 2007; Han et al., 2005; Cordero et al., 2010, 2012; Niordson and Kysar, 2014; Wulfinghoff et al., 2015).

In between these two formulations (DDD and continuum phenomenological strain gradient plasticity), another continuum approach, called phenomenological Mesoscopic Field Dislocation Mechanics (here abbreviated MFDM throughout the paper) has been proposed as an efficient method to model size-dependent plasticity at the mesoscopic scale (Acharya and Roy, 2006; Acharya et al., 2006; Roy and Acharya, 2006; Roy et al., 2007). This theory combines continuum dislocation mechanics theory and strain gradient crystal plasticity integrating the mobilities of both GNDs and SSDs (Acharya, 2001, 2003; Roy and Acharya, 2005; Acharya and Roy, 2006; Acharya, 2011). In this mesoscale theory, the constitutive equations for strain-hardening models, slip rule for SSD and velocity of GND need to be specified

phenomenologically. MFDM requires numerically solving the GND density transport equation together with stress balance field equation, which allows predicting the collective arrangement of GNDs and associated long range stresses. This was done with finite elements in Roy and Acharya (2005, 2006) and in Varadhan et al. (2006). Different size effects for single crystalline materials and multicrystalline thin films have been predicted with the MFDM theory as reported in Roy and Acharya (2006), Puri et al. (2009) and Puri et al. (2011). Grain size distribution and crystallographic orientation effects in multicrystalline thin films were discussed in Puri and Roy (2012). The role of GND density transport in ice single- or multi-crystals was studied in Taupin et al. (2007) and Richeton et al. (2017). Varadhan et al. (2009) and Gupta et al. (2017) coupled the MFDM equations with a dynamic strain aging model in order to predict the strain-aging behaviors of single crystalline and polycrystalline Al alloys. More recently, dislocation pattern formation and associated size effects was investigated by Arora and Acharya (2019) using finite deformation MFDM. However, all these contributions reported simulations on polycrystals with a small number of grains due to limiting CPU and memory requirements, needed to solve MFDM equations with the finite element method.

FFT-based methods were initially developed and further applied to composite materials (Moulinec and Suquet, 1994, 1998; Eyre and Milton, 1999; Michel et al., 2001), in which the heterogeneity is given by the spatial distribution of phases with different mechanical properties, and later adapted to polycrystals (Lebensohn, 2001), where the heterogeneity is related to the spatial distribution of anisotropic crystals with different orientations. This original CP-FFT implementation showed the feasibility of efficiently solving the micromechanical behavior of complex polycrystalline unit cells. Subsequent numerical implementations of the FFT-based method for polycrystals have been developed, for different constitutive descriptions of the behavior of each single crystal material point. The different constitutive regimes solved

with FFT-based methods include: linear elasticity (Lebensohn, 2001; Brenner et al., 2009); linear viscosity (Lebensohn et al., 2005); linear elasticity with eigenstrains or thermoelasticity (Vinogradov and Milton, 2008; Anglin et al., 2014; Donegan and Rollett, 2015; Eloh et al., 2019); rigid-viscoplasticity (Lebensohn, 2001; Lebensohn et al., 2008, 2009; Lee et al., 2011; Rollett et al., 2010); small-strain crystal plasticity elasto-viscoplasticity, i.e. CP-EVPFFT (Lebensohn et al., 2012; Grennerat et al., 2012; Suquet et al., 2012); large-strain elasto-viscoplasticity (Eisenlohr et al., 2013; Shanthraj et al., 2015; Kabel et al., 2016; Vidyasagar et al., 2018; Lucarini and Segurado, 2019); dilatational plasticity (Lebensohn et al., 2011, 2013); lower-order (Haouala et al., 2020) and higher-order (Lebensohn and Needleman, 2016) strain-gradient crystal plasticity; curvature-driven plasticity (Upadhyay et al., 2016); transformation plasticity (Richards et al., 2013; Otsuka et al., 2018); twinning (Mareau and Daymond, 2016; Paramatmuni and Kanjarla, 2019), fatigue (Rovinelli et al., 2017, 2018; Lucarini and Segurado, 2019); and quasi-brittle damage (Li et al., 2012; Sharma et al., 2012). FFT-based methods were also applied to field dislocation mechanics (FDM) and field disclination mechanics (Brenner et al., 2014; Berbenni et al., 2014; Djaka et al., 2015; Berbenni et al., 2016; Djaka et al., 2017; Berbenni and Taupin, 2018), and discrete dislocation dynamics (DDD) problems (Bertin et al., 2015; Graham et al., 2016; Bertin and Capolungo, 2018), providing the efficiency needed for the implementation of these powerful and numerically-demanding formulations.

In the case of polycrystalline materials, MFDM numerical implementation may take advantage of FFT-based methods, which were already proven to be numerically efficient for elasto-static FDM (Berbenni et al., 2014; Brenner et al., 2014; Djaka et al., 2017) and for the resolution of the dislocation density transport equation at constant applied GND velocity (Djaka et al., 2015) or together with stress equilibrium for two-phase laminate structures (Djaka et al., 2019). Therefore, the objective of

this paper is to develop an EVPFFT-based method for MFDM (named MFDM-EVPFFT throughout the paper) for describing grain size effects on flow stress of polycrystals at small strains due to both GNDs and SSDs and local GND dislocation density evolution in the course of monotonic and reversible plastic deformation. Specifically, we use MFDM-EVPFFT to study grain size effects on local mechanical fields of FCC polycrystalline aggregates and the role of GND densities and mobilities during a Bauschinger test. We aim at showing the effect of GND density pile ups as predicted by MFDM-EVPFFT on stress heterogeneity during reversible loading.

Starting from the EVPFFT formulation developed by Lebensohn et al. (2012), here designated as conventional CP-EVPFFT, MFDM-EVPFFT is based on a modified expression of the Jacobian for the augmented Lagrangian scheme, a spectral resolution of the dislocation density transport equation required by the MFDM theory and a hardening law accounting for GND density. A method based on finite differences and discrete Fourier transforms to treat both lattice incompatibility and integral Lippmann-Schwinger equations is used. The present work extends the preliminary study of Djaka et al. (2019) for laminate microstructures to polycrystalline microstructures and investigates how grain size affects intra-granular micromechanical fields like plastic strain, equivalent Von Mises stress and GND density. With that purpose, the effect of average grain size of idealized polycrystals with 27 and 100 grains and random orientations is studied. The tensile and tension-compression-tension (cyclic) responses of these polycrystals are simulated with the MFDM-EVPFFT model and are compared with CP-EVPFFT. The material parameters are the same as the ones used in Djaka et al. (2019) for Al-based laminate microstructures. No special interface conditions at grain boundaries are considered here, although such physically motivated interface conditions can be included in the MFDM theory (Acharya, 2007; Puri et al., 2011).

The paper is organized as follows: in section 2, the MFDM constitutive equations are summarized and the MFDM-EVPFFT formulation is presented. Section 3 presents an application of MFDM-EVPFFT to polycrystalline aggregates with different grain sizes and reversible (cyclic) plasticity to study the grain size dependence of the Bauschinger effect.

2 Theory and numerical spectral implementation

2.1 Notation

A bold symbol denotes a tensor or a vector. The symmetric part of tensor $\mathbf{A}$ is denoted $\mathbf{A}^{sym}$. Its skew-symmetric part is $\mathbf{A}^{skew}$. The tensor $\mathbf{A} \cdot \mathbf{B}$, with rectangular Cartesian components $A_{ik}B_{kj}$, results from the dot product of tensors $\mathbf{A}$ and $\mathbf{B}$, and $\mathbf{A} \otimes \mathbf{B}$ is their tensorial product, with components $A_{ij}B_{kl}$. The vector $\mathbf{A} \cdot \mathbf{V}$, with rectangular Cartesian components $A_{ij}V_j$, results from the dot product of tensor $\mathbf{A}$ and vector $\mathbf{V}$. The symbol " : " represents the trace inner product of the two second order tensors $\mathbf{A} : \mathbf{B} = A_{ij}B_{ij}$, in rectangular Cartesian components, or the product of a higher rank with a second rank tensor, e.g., $\mathbf{A} : \mathbf{B} = A_{ijkl}B_{kl}$. The cross product of a second rank tensor $\mathbf{A}$ and a vector $\mathbf{V}$, the **div** and **curl** operations for second rank tensors are defined row by row, in analogy with the vectorial case. For any base vector $\mathbf{e}_i$ of the reference frame:

$$(\mathbf{A} \times \mathbf{V})^t \cdot \mathbf{e}_i = (\mathbf{A}^t \cdot \mathbf{e}_i) \times \mathbf{V} \tag{1}$$
$$(\mathbf{div}\ \mathbf{A})^t \cdot \mathbf{e}_i = \mathbf{div}(\mathbf{A}^t \cdot \mathbf{e}_i) \tag{2}$$
$$(\mathbf{curl}\ \mathbf{A})^t \cdot \mathbf{e}_i = \mathbf{curl}(\mathbf{A}^t \cdot \mathbf{e}_i) \tag{3}$$

In rectangular Cartesian components:

$$(\mathbf{A} \times \mathbf{V})_{ij} = e_{jkl} A_{ik} V_l \tag{4}$$
$$(\mathbf{div}\mathbf{A})_i = A_{ij,j} \tag{5}$$
$$(\mathbf{curl}\,\mathbf{A})_{ij} = e_{jkl} A_{il,k} = -(\mathbf{grad}\,\mathbf{A} : \mathbf{X})_{ij} \tag{6}$$

where e_{jkl} is a component of the third rank alternating Levi-Civita tensor $\mathbf{X}$ and the spatial derivative with respect to a Cartesian coordinate is indicated by a comma followed by the component index. The notation $\widehat{\mathbf{A}}(\boldsymbol{\xi})$ will be used for the Fourier transform of $\mathbf{A}(\boldsymbol{x})$. Other notations will be specified in the text.

2.2 Constitutive equations of the reduced MFDM theory

To obtain the displacement $\mathbf{u}$, the strain $\boldsymbol{\varepsilon}$ and the stress $\boldsymbol{\sigma}$ fields using fast Fourier transform-based micromechanics, a small deformation setting is considered for elasto-viscoplastic materials with periodic microstructure. The field equations are solved at any point $\mathbf{x}$ of a unit cell V with periodic boundary conditions:

$$\begin{aligned} &\mathbf{div}\,\boldsymbol{\sigma} = 0 \\ &\boldsymbol{\sigma} = \mathbf{C} : \boldsymbol{\varepsilon}^e \\ &\mathbf{U} = \mathbf{grad}\,\mathbf{u} = \mathbf{U}^e + \mathbf{U}^p \\ &\mathbf{u} - < \boldsymbol{\varepsilon} > \cdot \mathbf{x} \text{ periodic, } \boldsymbol{\sigma} \cdot \mathbf{n} \text{ anti-periodic} \end{aligned} \tag{7}$$

where $< \cdot >$ denotes a volume average over V, $\boldsymbol{\varepsilon}^e = (\mathbf{U}^e)^{sym}$ and $\mathbf{C}$ is the fourth order elastic stiffness tensor with classic minor and major symmetries, which is known at each point $\mathbf{x}$ of V. Generally, macroscopic strain $< \boldsymbol{\varepsilon} >= \mathbf{E}$ or stress $< \boldsymbol{\sigma} >= \boldsymbol{\Sigma}$ (or mixed ones) are prescribed.

In the presence of dislocation ensembles both the average plastic distortion $\mathbf{U}^p$, which results from dislocation motion, and the average elastic (or lattice) distortion $\mathbf{U}^e$ are incompatible fields. In non local crystal plasticity and depending on the resolution scale, dislocation ensembles can be categorized as GNDs (Ashby, 1970)

and SSDs. The mesoscale FDM theory is based on an average value of the Nye tensor $\boldsymbol{\alpha}$ describing GND density, which is here considered as a periodic field. Here, a simplified version of the MFDM is considered (Acharya and Roy, 2006; Roy et al., 2007), such that the average plastic distortion rate writes:

$$\dot{\mathbf{U}}^p = \boldsymbol{\alpha} \times \mathbf{v} + \mathbf{L}^p \tag{8}$$

The mobility of SSDs is represented by the mesoscale plastic distortion rate denoted $\mathbf{L}^p$ where the averaging procedure was defined in Acharya and Roy (2006). The space-time evolution of the average dislocation density tensor $\boldsymbol{\alpha}$ is prescribed as:

$$\dot{\boldsymbol{\alpha}} = -\mathbf{curl}\ \dot{\mathbf{U}}^p \tag{9}$$

Constitutive specifications on the dislocation velocity $\mathbf{v}$ and on the slip distortion rate $\mathbf{L}^p$ are obtained from thermodynamic considerations, see Acharya and Roy (2006) for details. Furthermore, plastic flow incompressibility is considered, i.e. $L^p_{ii} = 0$ and $e_{ikl}\alpha_{ik}v_l = 0$. The GND velocity $\mathbf{v}$ is prescribed as follows:

$$\mathbf{v} = \frac{\mathbf{g}}{|\mathbf{g}|}v \quad \text{with} \quad v \geq 0 \tag{10}$$

where $\mathbf{g}$ is the glide force parallel to $\mathbf{v}$ and v is the magnitude of $\mathbf{v}$. The constitutive equation adopted for v is based on Orowan law for GND mobile dislocations:

$$v = \frac{\eta^2\, b}{N}\left(\frac{\mu}{\tau_c}\right)^2 \sum_{s=1}^{N} |\dot{\gamma}^s| \tag{11}$$

where N is the total number of slip systems ($N = 12$ for FCC metals), $\dot{\gamma}^s$ is the slip rate on slip system s, η is a material constant close to 1/3 (Ashby, 1970), b is the magnitude of the Burgers vector, τ_c is the resolved shear strength and μ is the isotropic elastic shear modulus of the material. Furthermore, $\mathbf{g}$ writes in component form (see details in Acharya and Roy (2006) and in Djaka et al. (2019)):

$$g_r = e_{ikr}\alpha_{jk}s_{ij} - e_{ikr}\alpha_{ik}\frac{s_{mn}\alpha_{np}(\alpha_{mp} - \alpha_{pm})}{\alpha_{ij}(\alpha_{ij} - \alpha_{ji})}, \tag{12}$$

where $s_{ij} = \sigma_{ij} - \frac{1}{3}\sigma_{kk}\delta_{ij}$ denotes the deviatoric stress tensor.

Plastic distortion rate tensor $\mathbf{L}^p$ due to slip from SSDs is defined as:

$$\mathbf{L}^p = \sum_{s=1}^{N} \dot{\gamma}^s \mathbf{b}^s \otimes \mathbf{n}^s = \sum_{s=1}^{N} \dot{\gamma}^s \mathbf{m}^s, \tag{13}$$

where $\mathbf{m}^s$ is the non-symmetric Schmid tensor defined as $\mathbf{m}^s = \mathbf{b}^s \otimes \mathbf{n}^s$. For each slip system s, the unit vector $\mathbf{b}^s$ denotes the slip direction and $\mathbf{n}^s$ the slip plane unit normal. The constitutive equation for $\dot{\gamma}^s$ introduced in eqs. 11 and 13 is given by a classic power law:

$$\dot{\gamma}^s = \dot{\gamma}^0 \left(\frac{|\tau^s|}{\tau_c} \right)^{1/m} sgn(\tau^s) \tag{14}$$

where m is the strain rate sensitivity of the material, $\tau^s = \mathbf{m}^s : \boldsymbol{\sigma}$ is the resolved shear stress, $\dot{\gamma}^0$ is a reference slip rate and τ_c is considered identical for all slip systems. The cumulated slip rate on all slip systems is given by:

$$\dot{\Gamma} = |\boldsymbol{\alpha} \times \mathbf{v}| + \sum_{s=1}^{N} |\dot{\gamma}^s| \tag{15}$$

where $|\boldsymbol{\alpha} \times \mathbf{v}|$ is the Euclidian norm of $\boldsymbol{\alpha} \times \mathbf{v}$.

The evolution law for the shear strength τ_c follows the same hypotheses as the strain-hardening models developed by Acharya and Roy (2006), Puri et al. (2011) and Djaka et al. (2019):

$$\dot{\tau}_c = \theta_0 \frac{\tau_s - \tau_c}{\tau_s - \tau_0} \dot{\Gamma} + k_0 \frac{\eta^2 \mu^2 \, b}{2\,(\tau_c - \tau_0)} \left(\sum_{s=1}^{N} |\boldsymbol{\alpha} \cdot \mathbf{n}^s| \, |\dot{\gamma}^s| + \sum_{s=1}^{N} |\boldsymbol{\alpha} \cdot \mathbf{n}^s| \, |\boldsymbol{\alpha} \times \mathbf{v}| \right) \tag{16}$$

where τ_0 is the yield strength due to lattice friction (which is low for FCC metals), τ_s is the saturation stress, θ_0 is the stage II hardening rate for FCC metals, k_0 is related to a geometric mean free path due to GND forest on slip system s. In eq. 16, $|\boldsymbol{\alpha} \cdot \mathbf{n}^s|$ is the L^2 norm of $\boldsymbol{\alpha} \cdot \mathbf{n}^s$.

For the space-time evolution of the dislocation density tensor (see eq. 9), an explicit forward Euler scheme was implemented to numerically solve this equation using a

Taylor expansion at first order of $\alpha_{ij}^{t+\triangle t}$ where $\triangle t$ is the time step, see Varadhan et al. (2006) and Djaka et al. (2015) for details.

2.3 MFDM-EVPFFT numerical implementation

An elasto-viscoplastic crystal plasticity formulation is adopted in a small deformation setting. Using a backward Euler implicit time discretization and the generalized Hooke's law, the expression of the stress tensor $\boldsymbol{\sigma}$ at $t + \triangle t$ is given by:

$$\boldsymbol{\sigma}^{t+\triangle t} = \mathbf{C} : \boldsymbol{\varepsilon}^{e,t+\triangle t} = \mathbf{C} : \left(\boldsymbol{\varepsilon}^{t+\triangle t} - \boldsymbol{\varepsilon}^{p,t} - \dot{\boldsymbol{\varepsilon}}^{p,t+\triangle t}(\boldsymbol{\sigma}^{t+\triangle t})\triangle t\right), \tag{17}$$

In what follows, the supra-indices $t + \triangle t$ are omitted for sake of simplicity, and only the fields corresponding to the previous time step t will be explicitly indicated. The unknown total strain field $\boldsymbol{\varepsilon}$ is solved through an integral Lippmann-Schwinger equation:

$$\boldsymbol{\varepsilon}(\mathbf{x}) = \langle\boldsymbol{\varepsilon}\rangle - \int_V \boldsymbol{\Gamma}^0(\mathbf{x} - \mathbf{x}') : \boldsymbol{\tau}(\mathbf{x}')dV' \tag{18}$$

where $\langle\boldsymbol{\varepsilon}\rangle$ represents the average value of $\boldsymbol{\varepsilon}$ in V, $\boldsymbol{\Gamma}^0$ is the Green operator associated with the homogeneous elastic moduli $\mathbf{C}^0$ and $\boldsymbol{\tau} = \boldsymbol{\sigma} - \mathbf{C}^0 : \boldsymbol{\varepsilon}$ is the stress polarization field. In the following, eq. 18 is solved using the FFT-based augmented Lagrangian scheme introduced by Michel et al. (2001). As in Lebensohn and Needleman (2016), the homogeneous elastic moduli tensor is taken as the Voigt average of $\mathbf{C}(\mathbf{x})$ over the unit cell V such that $\mathbf{C}^0 = \langle\mathbf{C}\rangle$.

In Fourier space, $\boldsymbol{\xi}$ is the Fourier vector of magnitude $\xi = \sqrt{\boldsymbol{\xi}\cdot\boldsymbol{\xi}}$ and components ξ_i. The imaginary unit is $\mathrm{i} = \sqrt{-1}$. Let $\widehat{\boldsymbol{\varepsilon}}(\boldsymbol{\xi})$ and $\widehat{\boldsymbol{\Gamma}}^0(\boldsymbol{\xi})$ be, respectively, the Fourier transform of $\boldsymbol{\varepsilon}(\boldsymbol{x})$ and $\boldsymbol{\Gamma}^0(\mathbf{x})$. The Fourier transform of the integral Lippmann-

Schwinger equation (eq. 18) yields:

$$\begin{aligned} \widehat{\boldsymbol{\varepsilon}}(\boldsymbol{\xi}) &= -\widehat{\boldsymbol{\Gamma}}^0(\boldsymbol{\xi}) : \widehat{\boldsymbol{\tau}}(\boldsymbol{\xi}) \ \forall \boldsymbol{\xi} \neq \mathbf{0} \\ \widehat{\boldsymbol{\varepsilon}}(\mathbf{0}) &= \langle \boldsymbol{\varepsilon} \rangle \end{aligned} \tag{19}$$

The calculation of the components of the Green operator in Fourier space $\widehat{\Gamma}^0_{ijkl}$ as part of the solution of the Lippmann-Schwinger equation is performed using a centered finite difference scheme on a rotated grid introduced by Willot (2015), see also Djaka et al. (2017, 2019).

Let us assume now that $\lambda^{(\mathrm{n})}_{ij}$ and $e^{(\mathrm{n})}_{ij}$ are, respectively, the auxiliary guess stress and strain fields at iteration (n). The stress polarization tensor becomes: $\tau^{(\mathrm{n})}_{ij} = \lambda^{(\mathrm{n})}_{ij} - C^0_{ijkl} e^{(\mathrm{n})}_{kl}$. An alternative fixed-point expression, which requires computing the Fourier transform of the stress field instead of that of the polarization field was reported in Michel et al. (2001):

$$\begin{aligned} \widehat{e}^{(\mathrm{n}+1)}_{ij}(\boldsymbol{\xi}) &= \widehat{e}^{(\mathrm{n})}_{ij}(\boldsymbol{\xi}) - \widehat{\Gamma}^0_{ijkl}(\boldsymbol{\xi}) \widehat{\lambda}^{(\mathrm{n})}_{kl}(\boldsymbol{\xi}) \ \forall \boldsymbol{\xi} \neq \mathbf{0} \\ \widehat{e}^{(\mathrm{n}+1)}_{ij}(\mathbf{0}) &= \langle \varepsilon^{(\mathrm{n})}_{ij} \rangle \end{aligned} \tag{20}$$

Once $e^{(\mathrm{n}+1)}_{ij} = \mathrm{FFT}^{-1}(\widehat{e}^{(\mathrm{n}+1)}_{ij}(\boldsymbol{\xi}))$ is obtained in the real space by using the inverse Fourier transform (FFT^{-1}), the nullification of the residual $\mathbf{R}$, which depends on the stress and strain tensors $\boldsymbol{\sigma}^{(\mathrm{n}+1)}$ and $\boldsymbol{\varepsilon}^{(\mathrm{n}+1)}$, is solved:

$$R_{ij}(\boldsymbol{\sigma}^{(\mathrm{n}+1)}) = \sigma^{(\mathrm{n}+1)}_{ij} + C^0_{ijmn} \varepsilon^{(\mathrm{n}+1)}_{mn}(\boldsymbol{\sigma}^{(\mathrm{n}+1)}) - \lambda^{(\mathrm{n})}_{ij} - C^0_{ijmn} e^{(\mathrm{n}+1)}_{mn} = 0 \tag{21}$$

This nonlinear equation was solved by Lebensohn et al. (2012) using a Newton-Raphson type scheme. The $(\mathrm{p}+1)$-guess for the stress field $\boldsymbol{\sigma}^{(\mathrm{n}+1)}_{ij}$ is given by:

$$\sigma^{(\mathrm{n}+1,\mathrm{p}+1)}_{ij} = \sigma^{(\mathrm{n}+1,\mathrm{p})}_{ij} - \left(\left(\frac{\partial R_{ij}}{\partial \sigma_{mn}} \right)_{\boldsymbol{\sigma}^{(\mathrm{n}+1,\mathrm{p})}} \right)^{-1} R_{mn}\left(\boldsymbol{\sigma}^{(\mathrm{n}+1,\mathrm{p})} \right) \tag{22}$$

Using the constitutive specifications, the Jacobian in the above expression reads:

$$\left(\frac{\partial R_{ij}}{\partial \sigma_{mn}}\right)_{\boldsymbol{\sigma}^{(\mathrm{n+1,p})}} = \delta_{im}\delta_{jn} + C^0_{ijkl}C^{-1}_{klmn} + \triangle t\, C^0_{ijkl}\left(\frac{\partial \dot{\varepsilon}^p_{kl}}{\partial \sigma_{mn}}\right)_{\boldsymbol{\sigma}^{(\mathrm{n+1,p})}} \tag{23}$$

The expression of $\partial \dot{\varepsilon}^p_{kl}/\partial \sigma_{mn}$ considering the constitutive equations of the MFDM theory yields (Djaka et al., 2019):

$$\left(\frac{\partial \dot{\varepsilon}^p_{kl}}{\partial \sigma_{mn}}\right)_{\boldsymbol{\sigma}^{(\mathrm{n+1,p})}} = \frac{1}{2}\left(\frac{\partial L^p_{kl}}{\partial \sigma_{mn}} + \frac{\partial L^p_{lk}}{\partial \sigma_{mn}}\right)_{\boldsymbol{\sigma}^{(\mathrm{n+1,p})}} + \frac{1}{2}\left(\frac{\partial\left(\alpha \times v\right)_{kl}}{\partial \sigma_{mn}} + \frac{\partial\left(\alpha \times v\right)_{lk}}{\partial \sigma_{mn}}\right)_{\boldsymbol{\sigma}^{(\mathrm{n+1,p})}} \tag{24}$$

An approximation expression of $\partial L^p_{kl}/\partial \sigma_{mn}$ is given by:

$$\left(\frac{\partial L^p_{kl}}{\partial \sigma_{mn}}\right)_{\boldsymbol{\sigma}^{(\mathrm{n+1,p})}} \simeq n\dot{\gamma}^0 \sum_{s=1}^{N} m^s_{kl} P^s_{mn} \frac{\left|P^s_{mn}\sigma_{mn}\right|^{n-1}}{(\tau_c)^n} \tag{25}$$

where $\mathbf{P}^s = (\mathbf{m}^s)^{sym}$ is the symmetric Schmid tensor. The determination of the expression of $\partial\left(\alpha \times v\right)_{kl}/\partial \sigma_{mn}$ is an addition to the standard EVPFFT formulation and is computed as follows (Djaka et al., 2019):

$$\left(\frac{\partial(\alpha \times v)_{kl}}{\partial \sigma_{mn}}\right)_{\boldsymbol{\sigma}^{(\mathrm{n+1,p})}} = e_{lqr}\alpha_{kq}\left(\frac{\partial\left(g_r/|\mathbf{g}|\right)}{\partial \sigma_{mn}} v + \frac{g_r}{|\mathbf{g}|}\frac{\partial v}{\partial \sigma_{mn}}\right)_{\boldsymbol{\sigma}^{(\mathrm{n+1,p})}} \tag{26}$$

with, using eq. 12:

$$\begin{aligned}\frac{\partial\left(g_r/|\mathbf{g}|\right)}{\partial \sigma_{mn}} = &\left(\frac{\delta_{rs}|\mathbf{g}|^2 - g_r g_s}{|\mathbf{g}|^3}\right)\left(e_{oks}\alpha_{qk} - e_{iks}\alpha_{ik}\frac{\alpha_{qp}(\alpha_{op}-\alpha_{po})}{\alpha_{ij}(\alpha_{ij}-\alpha_{ji})}\right)\\ &\left(\delta_{om}\delta_{qn} - \frac{1}{3}\delta_{mn}\delta_{oq}\right)\end{aligned} \tag{27}$$

and:

$$\left(\frac{\partial v}{\partial \sigma_{mn}}\right)_{\boldsymbol{\sigma}^{(\mathrm{n+1,p})}} \simeq n\dot{\gamma}^0 \frac{\eta^2\, b}{N}\left(\frac{\mu}{\tau_c}\right)^2 \sum_{s=1}^{N} P^s_{mn} \frac{\left|P^s_{mn}\sigma_{mn}\right|^{n-1}}{(\tau_c)^n} \tag{28}$$

In eqs. 25 and 28, the approximation lies in the fact that the derivatives $\partial \tau_c/\partial \boldsymbol{\sigma}$ and $\partial \mathbf{P}^s/\partial \boldsymbol{\sigma}$ are neglected.

Once the convergence is achieved on $\boldsymbol{\sigma}^{(\mathrm{n+1})}$ and $\boldsymbol{\varepsilon}^{(\mathrm{n+1})}$, the new guess for the auxiliary stress field $\boldsymbol{\lambda}$ is given using the Uzawa descent algorithm:

$$\lambda^{(\mathrm{n+1})}_{ij} = \lambda^{(\mathrm{n})}_{ij} + C^0_{ijkl}\left(e_{kl}{}^{(\mathrm{n+1})} - \varepsilon_{kl}{}^{(\mathrm{n+1})}\right) \tag{29}$$

and the algorithm is stopped when the normalized average differences between the stress fields $\boldsymbol{\sigma}$ and $\boldsymbol{\lambda}$, and the strain fields $\boldsymbol{\varepsilon}$ and $\mathbf{e}$, are smaller than a given threshold error (typically 10^{-5}). Following Lebensohn et al. (2012), this condition implies the fulfillment of both stress equilibrium and strain compatibility up to sufficient accuracy.

In the algorithm described above, an overall macroscopic strain $\mathbf{E} = \langle \boldsymbol{\varepsilon}^{(\mathrm{n})} \rangle$ is applied to the periodic unit cell V in the form of:

$$E_{ij} = E_{ij}^{t} + \dot{E}_{ij} \triangle t \tag{30}$$

In cases of mixed boundary conditions with imposed macroscopic strain rate $\dot{E}_{ij}$ and stress Σ_{ij}, the (n + 1)-guess of the macroscopic strain $E_{ij}^{(\mathrm{n}+1)}$ was given in Michel et al. (2001) and Lebensohn et al. (2012).

The direct and the inverse Fourier transforms are computed here by using Fast Fourier Transform (FFT) algorithm. The spatial periods of the unit cell are T_1, T_2 and T_3 in the x_1, x_2 and x_3 directions, respectively, and discretized by a regular rectangular grid with $N_1 \times N_2 \times N_3$ voxels with position vector $\mathbf{x} = (i_1\delta_1, i_2\delta_2, i_3\delta_3)$, where $i_1 = 0 \rightarrow N_1 - 1$, $i_2 = 0 \rightarrow N_2 - 1$, $i_3 = 0 \rightarrow N_3 - 1$ and δ_1, δ_2, δ_3 are the voxel sizes in the x_1, x_2 and x_3 directions (here $\delta_1 = \delta_2 = \delta_3 = \delta$). The computational grid is constituted of a total of $N_{tot} = N_1 \times N_2 \times N_3$ voxels.

Let $\widehat{\boldsymbol{\alpha}}(\boldsymbol{\xi})$ be the Fourier transform of $\boldsymbol{\alpha}(\mathbf{x})$. Following Djaka et al. (2015, 2019), the components of the Nye tensor are updated in the Fourier space as:

$$\widehat{\alpha}_{ij}^{t+\triangle t} = \kappa\left(\boldsymbol{\eta}\right)\left(\widehat{\alpha}_{ij}^{t} - \triangle t \ \mathrm{i}\ \xi_k \ \left(\widehat{\left(\alpha_{ij} v_k\right)}^{t} - \widehat{\left(\alpha_{ik} v_j\right)}^{t}\right)\right) - \triangle t \ \mathrm{i}\ \xi_k \ e_{jkl} \widehat{\left(L_{il}^{p}\right)}^{t} \tag{31}$$

where an exponential second order spectral low-pass filter $\kappa\left(\boldsymbol{\eta}\right)$ is used to stabilize the numerical approximation. This spectral filter allows eliminating high frequencies responsible for spurious oscillations. The exponential filter is defined as function of

discrete frequencies $\eta_j = m_j/N_j$ with $\xi_j = 2\pi m_j/T_j$ (Djaka et al., 2015, 2019):

$$\kappa\left(\frac{m_1}{N_1}, \frac{m_2}{N_2}, \frac{m_3}{N_3}\right) = \exp\left(-\beta\left(\left(\frac{m_1}{N_1}\right)^{2p} + \left(\frac{m_2}{N_2}\right)^{2p} + \left(\frac{m_3}{N_3}\right)^{2p}\right)\right), \tag{32}$$

where m_j $(j = 1 \rightarrow 3)$ are arranged in Fourier space as follows (Moulinec and Suquet, 1998):

$$m_j = \left(\left(-\frac{N_j}{2} + 1\right), \left(-\frac{N_j}{2} + 2\right), ..., -1, 0, 1, ..., \left(\frac{N_j}{2} - 1\right), \left(\frac{N_j}{2}\right)\right) \tag{33}$$

if N_j is even, and

$$m_j = \left(\left(-\frac{N_j - 1}{2}\right), ..., -1, 0, 1, ..., \left(\frac{N_j - 1}{2}\right)\right) \tag{34}$$

if N_j is odd.

The damping parameter β is defined as $\beta = -\log\, \varepsilon_M$, where ε_M is a low value parameter that was optimized by Djaka et al. (2015). For applications, $\epsilon_M = 0.2$ and $p = 1$.

To fix the time step $\triangle t$ in eq. 31 in order to satisfy stability requirements for numerically solving the dislocation density transport equation, a user-specified fraction denoted $c = 0.25$ of Courant-Friedrichs-Lewy (CFL) limit is used such that:

$$\triangle t_{CFL} = c\frac{\delta}{v_{max}} \tag{35}$$

where δ is the voxel size and v_{max} is the maximal GND velocity. Finally, the time step is given by $\triangle t = \min\left(\triangle t_{CFL}, \triangle t_{\varepsilon}\right)$ where $\triangle t_{CFL}$ is defined in eq. 35 and the time step $\triangle t_{\varepsilon}$ is the classic time step used in EVPFFT.

2.4 Use of finite difference schemes for spatial derivatives

The need for better numerical performance and stability in spectral approaches to avoid spurious oscillations of the local fields, known as Gibbs phenomenon or

aliasing, motivated the development of modified Green operators for the calculation of the displacement field and gradients of the latter in Fourier space (Willot and Pellegrini, 2008). For this, a successful numerical strategy (Berbenni et al., 2014; Lebensohn and Needleman, 2016) based on earlier works (Müller, 1996, 1998; Dreyer et al., 1999) consists in approximating first and second derivatives in Cartesian space using finite difference (FD) schemes, and taking discrete Fourier transforms from these FD expressions. Among these FD-based schemes, we choose a modified discrete Green operator based on centered FD on a rotated grid proposed (Willot, 2015) and adopted in different subsequent FFT-based implementations (Djaka et al., 2017; Bertin and Capolungo, 2018; Lucarini and Segurado, 2019; Djaka et al., 2019; Haouala et al., 2020) given its good numerical performance. The FFT-resolution of the Lippmann-Schwinger used a DFT-scheme coupled to a rotated centered finite difference scheme. It was observed (Djaka et al., 2019) that in the MFDM-EVPFFT formulation, the latter scheme does not modify very much the number of Newton-Raphson iterations needed for numerical convergence of the augmented Lagrangian scheme in comparison with the CP-EVPFFT and lead to more accurate fields near discontinuities than when using the classic Green operator.

3 Application to polycrystalline aggregates: grain size effect and reversible plasticity

3.1 Material and simulation parameters

In the following numerical simulations, Al polycrystalline aggregates made of 100 grains or 27 grains resulting from periodic Voronoi tessellations are considered, see Fig. 1. The Voronoi polyhedra characterize the grains and their shapes. In the present study, two different voxelized polycrystalline RVE obtained with periodic Voronoi tessellations are used with different grain sizes: $128 \times 128 \times 128$ voxels (Fig. 1 (a)) and $64 \times 64 \times 64$ voxels (Fig. 1 (b)).The crystallographic orientations of the grains are randomly distributed and are characterized by three Euler-Bunge angles: ϕ_1, Φ, ϕ_2. Twelve $(111) < 110 >$ slip systems are considered. The microstructure is characterized by a single internal length scale parameter which is the average grain size denoted $\bar{d}$. The latter is deduced from H the period of the unit cell as $\bar{d} = H/\sqrt[3]{27}$ and $\bar{d} = H/\sqrt[3]{100}$ for RVE with 27 grains or 100 grains respectively. A similar procedure was used by Lebensohn and Needleman (2016) to generate 3D polycrystals with different mean grain sizes using periodic Voronoi tessellations.

The material parameters related to elastic constants (Al), slip rule, GND velocity ($\dot{\gamma}^0$, m and η) and hardening (τ_0, τ_s, θ_0 and k_0) are consistent with pure Al. Here, the parameters are the same as in Djaka et al. (2019) and a specific fit of experimental data has not been carried out. The Burgers vector magnitude for Al is $b = 2.86 \times 10^{-10} m$. The reference material parameters used for numerical simulations are reported in Table 1. As reported in eq. 7, periodic boundary conditions are used and the unit cell is submitted to tensile (resp. compression) loading in the x_3-direction at macroscopic strain rate $\dot{E}_{33} = 10^{-3} s^{-1}$ (resp. $\dot{E}_{33} = -10^{-3} s^{-1}$) with mixed macroscopic strain/stress boundary conditions. We have chosen $k_0 = 20$ fol-

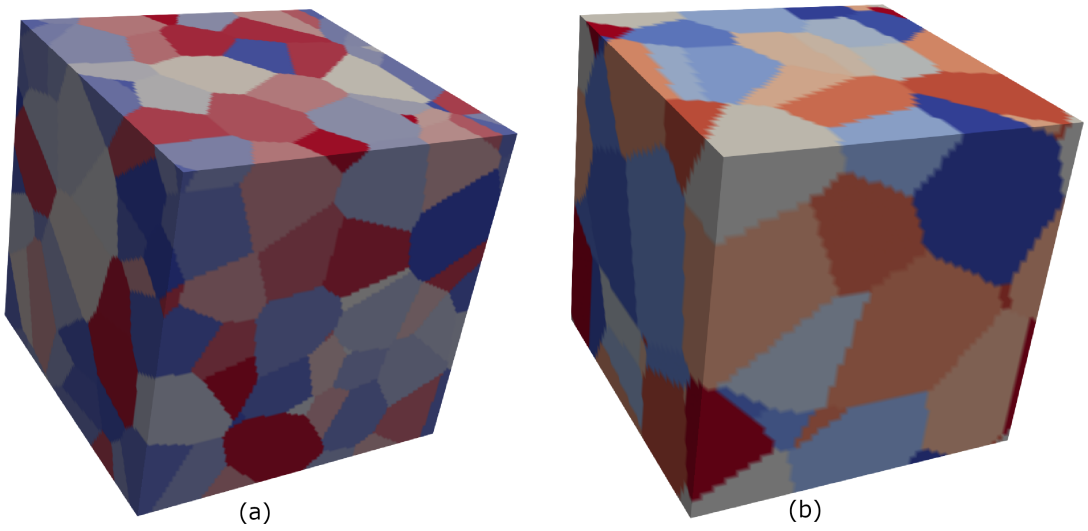

Figure 1. Different voxelized polycrystalline RVE obtained with periodic Voronoi tessellations and used for the present numerical simulations: 100 randomly oriented grains discretized with $128 \times 128 \times 128$ voxels (a) and 27 randomly oriented grains discretized with $64 \times 64 \times 64$ voxels (b).

lowing the value identified by Acharya and Beaudoin (2000) for the case of FCC polycrystals and by Roy and Acharya (2006) for MFDM. In the context of MFDM-EVPFFT, starting from $k_0 = 20$, the role of k_0 on overall strain hardening and GND density pile-ups was recently studied in Djaka et al. (2019) for two-phase laminate microstructures. For conventional crystal plasticity (CP-EVPFFT), the materials parameters used were the same except that $\boldsymbol{\alpha} = \mathbf{0}$ (no mobile GND density and no GND density in the strain-hardening law). However, in CP-EVPFFT, $\boldsymbol{\alpha}$ can be computed *a posteriori* using the definition of the Nye tensor in a small strain setting: $\boldsymbol{\alpha} = -\mathbf{curl}\, \mathbf{U}^p$ together with a centered finite difference scheme as detailed in Berbenni et al. (2014), Lebensohn and Needleman (2016) and Djaka et al. (2019).

Table 1

List of material parameters used for numerical simulations

E (GPa)	ν	$\dot{\gamma}^0(s^{-1})$	m	η	b (m)	τ_0 (MPa)	τ_s (MPa)	θ_0 (MPa)	k_0
69	0.33	1	0.05	0.33	2.86×10^{-10}	3	12	150	20

3.2 Overall grain size dependent responses

Here, a polycrystalline RVE with 100 or 27 randomly oriented grains is used for these numerical simulations with periodic Voronoi tessellations of $128 \times 128 \times 128$ voxels and $64 \times 64 \times 64$ voxels respectively. Polycrystals with different mean grain sizes $\bar{d}$ ranging from $0.25\mu m$ to $154.72\mu m$ are considered using the MFDM-EVPFFT model. The macroscopic tensile stress-strain curves are obtained and are compared to the results obtained from CP-EVPFFT simulations using same material parameters for slip rule and Kocks-Mecking's hardening law (Mecking and Kocks, 1981).

Using MFDM-EVPFFT in a plausible range of physical grain sizes for current metals and alloys, a grain size effect on the macroscopic tensile response of the Al polycrystalline aggregate is observed in Fig. 2(a) for the RVE constituted of 100 grains with $128 \times 128 \times 128$ voxels ($0.25\mu m$ to $100\mu m$) and in Fig. 2(b) for the RVE constituted of 27 grains with $64 \times 64 \times 64$ voxels ($0.25\mu m$ to $154.72\mu m$). Such size effect is not predicted using the conventional CP-EVPFFT that leads to grain size-insensitive response (see the dotted lines in Fig. 2(a,b)).

The scaling law for the macroscopic tensile flow stress as a function of the mean grain size $\bar{d}$ is now investigated in Fig. 3. For the chosen default material parameters reported in Table 1 and for these two polycrystalline RVEs (100 and 27 grains), a linear fit shows that a Hall-Petch law with exponent -0.5 is found for $\bar{d}$ ranging from $0.25\mu m$ to $154.72\mu m$. This figure shows that the overall tensile flow stress at $E^p_{33} =< \varepsilon^p_{33} >= 0.2\%$ is well fitted in this grain size range (with a square correlation coefficient close to 1) by the Hall-Petch's relationship for both RVEs:

$$< \sigma_{33} >=< \sigma^{\infty}_{33} > +K\bar{d}^n, \tag{36}$$

where $n = -0.5$, $< \sigma^{\infty}_{33} >= 20MPa$ (RVE: 100 grains) or $< \sigma^{\infty}_{33} >= 19.8MPa$ (RVE:

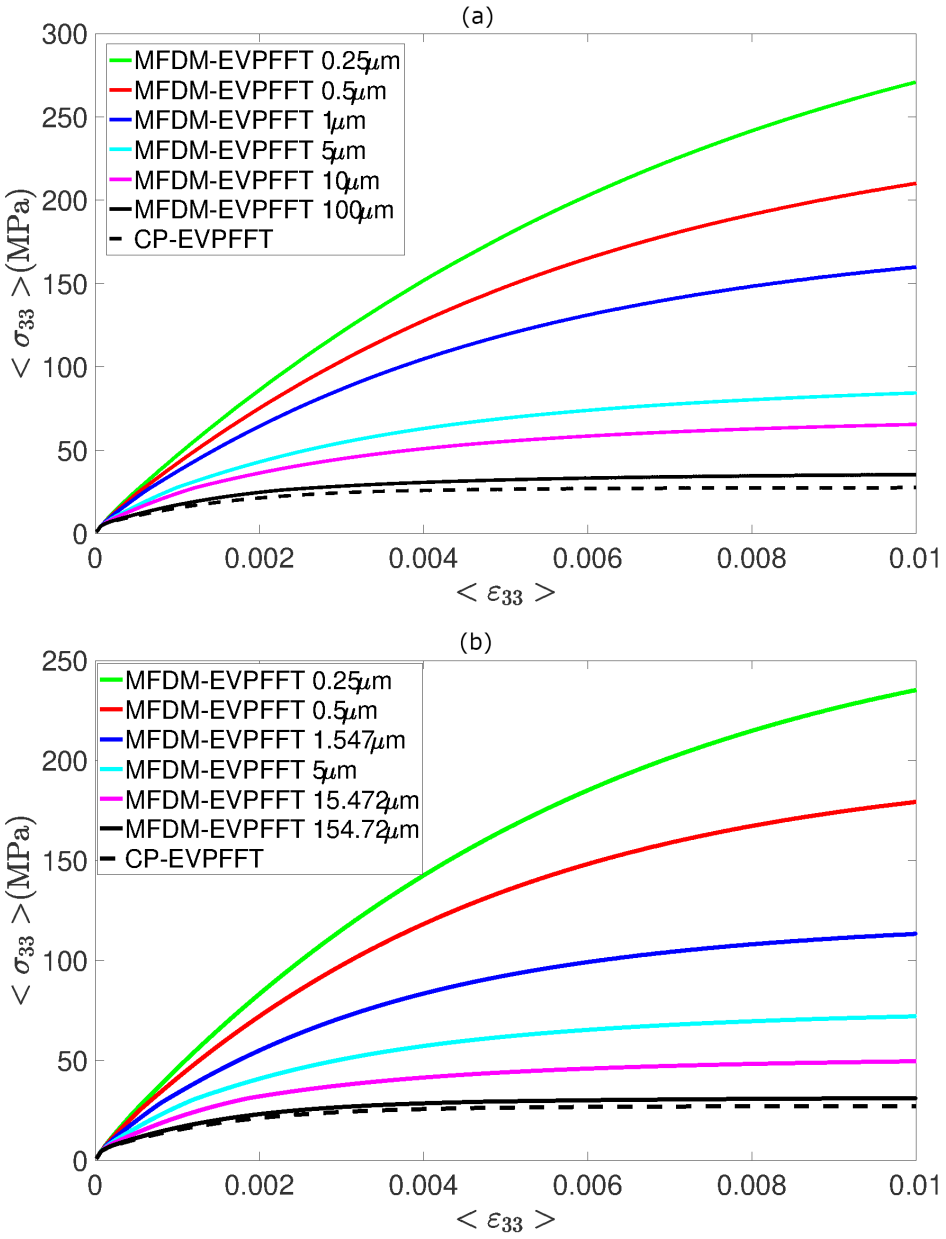

Figure 2. Grain size dependent tensile responses up to 1% strain for FCC polycrystals as predicted by the MFDM-EVPFFT formulation (solid lines) with grain sizes: (a) $\bar{d}$ ranging from $0.25\mu m$ to $100\mu m$ using a RVE of 100 randomly oriented grains with $128 \times 128 \times 128$ voxels, (b) $\bar{d}$ ranging from $0.25\mu m$ to $154.72\mu m$ using a RVE of 27 randomly oriented grains with $64 \times 64 \times 64$ voxels. For comparison, the tensile responses given by conventional plasticity (CP-EVPFFT) are also reported for both RVEs (dotted lines).

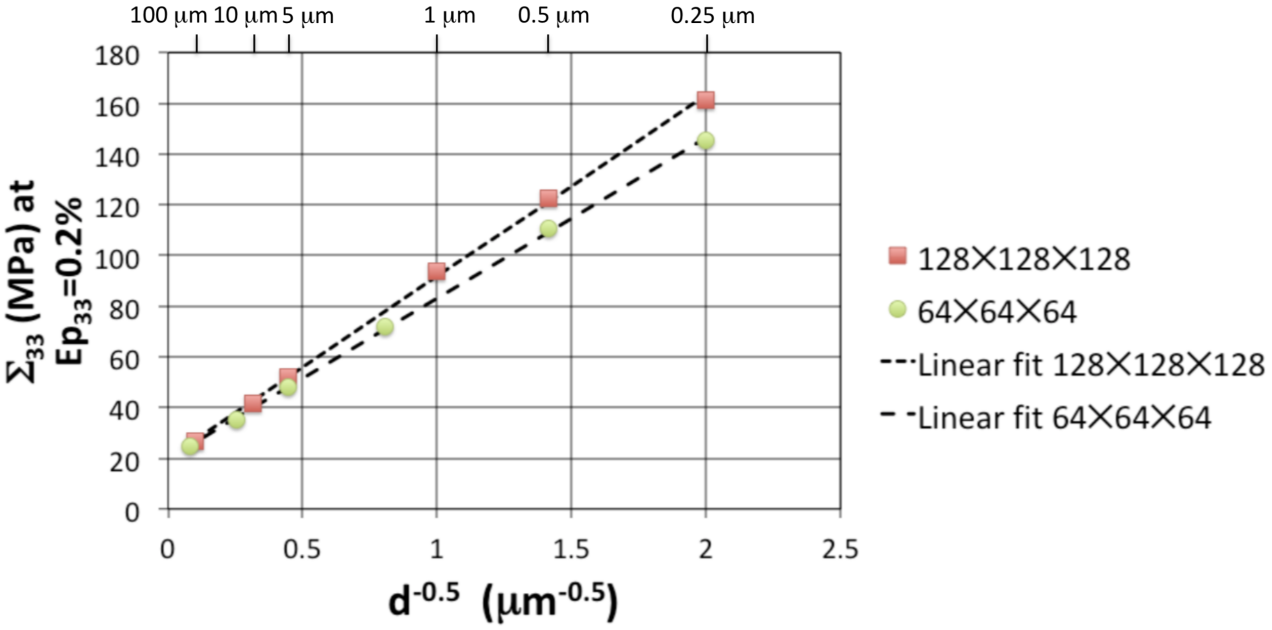

Figure 3. Grain size effect reported on the overall flow stress at 0.2% overall plastic strain ($E^p_{33} = 0.2\%$) and comparison with a Hall-Petch's type scaling law (linear fits: dotted lines). The numerical simulations are performed with the MFDM-EVPFFT formulation with a RVE of 100 grains and $128 \times 128 \times 128$ voxels and with a RVE of 27 grains and $64 \times 64 \times 64$ voxels.

27 grains) is the grain size independent flow stress that is obtained from conventional crystal plasticity (CP-EVPFFT), $K = 71.6 MPa.\mu m^{0.5}$ (RVE: 100 grains) or $K = 63.3 MPa.\mu m^{0.5}$ (RVE: 27 grains). Note that the size-dependent part $K\bar{d}^n$ is due to non local GND-based plasticity in the MFDM-EVPFFT and the values reported here for K and n appear to be realistic at low strains. However, we did not attempt to calibrate K (the so-called Hall-Petch's slope) and $< \sigma^{\infty}_{33} >$ directly from experimental data as reported for instance in Cordero et al. (2016), so that simulation predictions remain qualitative.

It is noteworthy that grain-size dependent behaviors for FCC polycrystals were also studied by other theories based on lower order strain gradient plasticity models (Acharya and Beaudoin, 2000; Cheong et al., 2005; Haouala et al., 2020) or based

on higher order strain gradient plasticity models (Ohno and Okumura, 2007; Ohno et al., 2008; Cordero et al., 2010, 2012; Lebensohn and Needleman, 2016). Using 3D FE simulations for Ni, Acharya and Beaudoin (2000) obtained the following scaling law $< \sigma > \propto K\bar{d}^{-4/5}$ at higher strains ($5\% - 20\%$) with average grain sizes ranging from $20\mu m$ to $200\mu m$. For Cu and Al, Cheong et al. (2005) performed 3D FE simulations with the commercial code ABAQUS and found a scaling law as $< \sigma > \propto K\bar{d}^{-1/2}$ at low strains (0.2%) based on a non local GND-based crystallographic model first developed by Busso et al. (2000). To fit the Hall-Petch's curves, these authors also consider the role of initial dislocation densities present at grain boundaries using different SSD densities. Recently, Haouala et al. (2020) also simulated the Hall-Petch effect in different FCC polycrystalline metals (Cu, Al, Ag, Ni) using a FFT-based Galerkin approach for lower strain gradient crystal plasticity. For a grain size range $\bar{d}$ between $10\mu m$ and $80\mu m$, they obtained a Hall-Petch's relationship depending on the initial dislocation density in the material and a scaling law for Al as $\bar{d}^n$ with $n = -0.69$ and $n = -0.59$ for overall strains of 1% and 5% respectively. In the case of higher order stress theories and due to the large number of degrees of freedom involved in these theories, only two-dimensional RVEs with 2D periodic Voronoi tessellations (Cordero et al., 2012) or 2D unit cells with 16 hexagonal grains (Ohno et al., 2008) were considered with the FE method assuming periodic boundary conditions. Therefore, crystal plasticity was limited to 2D planar double slip. This limitation may modify the scaling law compared to simulations considering 3D polycrystals. Using single spherical or tetrakaidecahedron model grains and the higher order stress model of Gurtin (2002), Ohno and Okumura (2007) found a grain size effect on the flow stress at 0.2% strain resulting from self-energy of GND and a scaling law as $< \sigma > \propto K\bar{d}^{-1}$ (for $\bar{d}$ larger than $\bar{d} = 0.1\mu m$). In Ohno et al. (2008), a strong grain size effect was reported on 2D polycrystals but only three mean grain sizes ($\bar{d} = 1\mu m$, $10\mu m$, $100\mu m$) were considered in their FE simulations but the scaling

law was not reported. It is interesting to compare predictions of the present model with the 2D numerical results of Cordero et al. (2012) for polycrystals deformed at low strains. Like in Cordero et al. (2012), the present 3D MFDM-EVPFFT simulation results exhibit a Hall-Petch's relationship for the flow stress at low strains. In the model of Cordero et al. (2012), the Hall-Petch's exponent was identified in a phenomenological way by calibrating the generalized moduli relating higher order stresses to micro-deformations.

3.3 Grain size dependence of intra-granular mechanical fields

Let us now study grain size effect on the spatial distribution of intra-granular mechanical fields. To that purpose, three mechanical field outputs are particularly analyzed:

(i) the Von Mises equivalent stress σ_{eq} to study stress hotspots in the polycrystalline aggregate. The Von Mises equivalent stress σ_{eq} is defined as:

$$\sigma_{eq} = \sqrt{\frac{3}{2}\mathbf{s} : \mathbf{s}} \tag{37}$$

where $\mathbf{s}$ is the deviatoric stress tensor.

(ii) the equivalent cumulated plastic strain ε^p_{eq} to study plastic strain localization in the polycrystal. ε^p_{eq} is defined as:

$$\varepsilon^p_{eq} = \int_0^t \sqrt{\frac{2}{3}\dot{\boldsymbol{\varepsilon}}^p : \dot{\boldsymbol{\varepsilon}}^p}\, dt \tag{38}$$

where $\dot{\boldsymbol{\varepsilon}}^p$ is the symmetric part of $\dot{\mathbf{U}}^p$.

(iii) the scalar GND density ρ_{GND} defined from the Nye tensor $\boldsymbol{\alpha}$ as:

$$\rho_{GND} = \frac{\sqrt{\boldsymbol{\alpha} : \boldsymbol{\alpha}}}{b} \tag{39}$$

The examination of the spatial distribution of this scalar GND density is preferred to the full analysis of each particular tensor components (9 components).

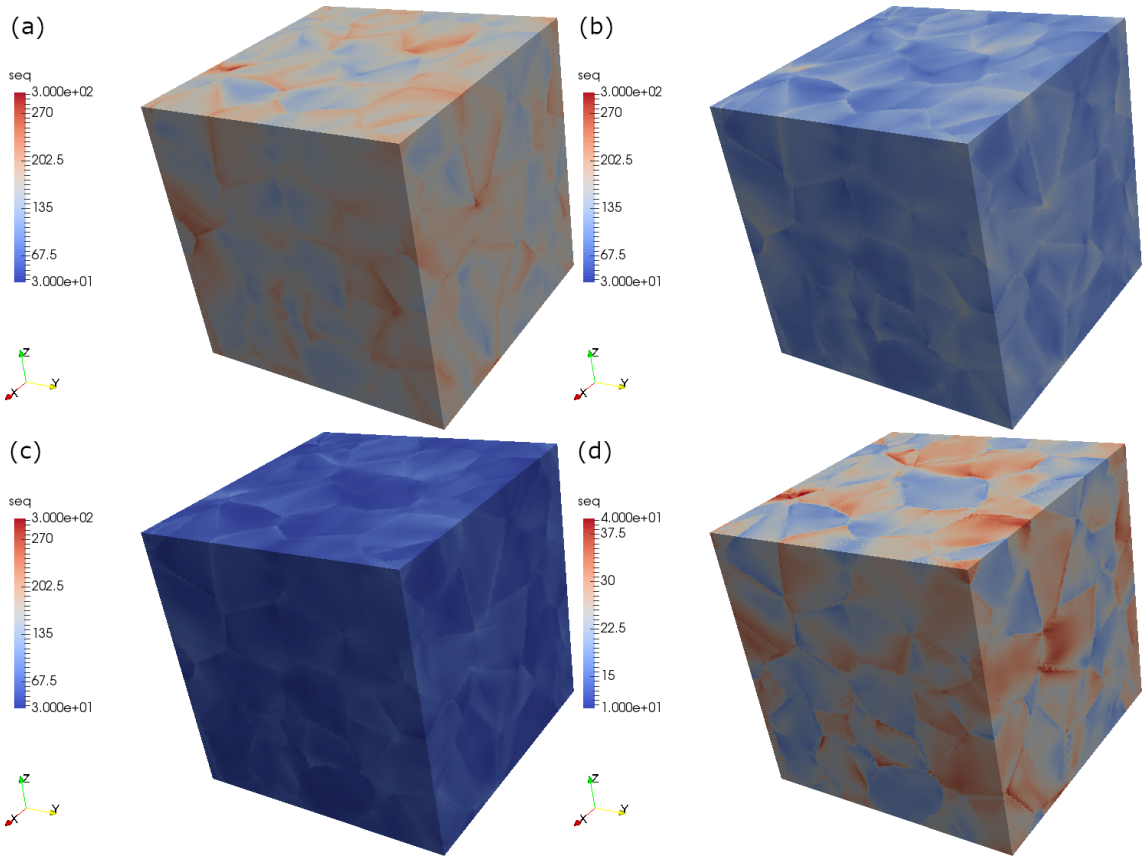

Figure 4. Spatial distribution of equivalent Von Mises stress σ_{eq} in MPa recorded at $E^p_{33} = 0.2\%$ for three grain sizes $\bar{d}$ (MFDM-EVPFFT) with same scale range: $0.25\mu m$ (a), $1\mu m$ (b), $10\mu m$ (c). Simulation results with CP-EVPFFT (d). The scale range for CP-EVPFFT is different to show the detailed fields.

Three average grain sizes $\bar{d}$ are considered for a RVE with $128 \times 128 \times 128$ voxels (100 grains): $0.25\mu m$, $1\mu m$, $10\mu m$. The mechanical fields are all recorded at the same overall plastic strain: $E^p_{33} = 0.2\%$. The contour plots of σ_{eq} expressed in MPa are reported on Fig. 4.

At lowest grain size ($\bar{d} = 0.25\mu m$) (Fig. 4(a)), it is seen that the equivalent Von Mises stress is inhomogeneous and localized in strong stress hotspots at grain boundary regions or near triple junctions. Strong stress gradients are also observed from grain boundaries or triple junctions to grain interiors with non local MFDM-EVPFFT formulation. At larger grain sizes ($\bar{d} = 10\mu m$, Fig. 4(c)), the stress is less localized

and stress hot spots gradually disappear for the same used stress scale range for contour plots. Fig. 4(d) shows the stress σ_{eq} given by CP-EVPFFT. The latter leads to more homogeneous intra-granular stress field. In addition, undesirable checker-board patterns are visible inside grains on the stress field with CP-EVPFFT. This phenomenon is absent with MFDM-EVPFFT, which leads to smoother spatial field variations. Both formulations use finite difference schemes for calculating spatial derivatives in the Fourier space, which shows that this difference only comes from the non local MFDM-EVPFFT formulation. A similar trend was also observed with the non local SG-EVPFFT formulation developed by Lebensohn and Needleman (2016).

The equivalent Von Mises stress statistics extracted from MFDM-EVPFFT are provided using 100 bin values. Fig. 5 reports the histograms of σ_{eq} (Fig. 5(a)) and σ_{eq}/Σ_{eq} (Fig. 5(b)) as a function of average grain size $\bar{d}$, where $\Sigma_{eq} =< \sigma_{eq} >$ is the volume average of σ_{eq} over the RVE. For comparisons, the statistics on σ_{eq} and σ_{eq}/Σ_{eq} using CP-EVPFFT local formulation are also reported on Fig. 5. It is first shown that the distributions of σ_{eq} are quite heterogeneous and the stress amplitudes between the maximal and minimal values increase as $\bar{d}$ decreases using the MFDM-EVPFFT formulation. The stress amplitude given by conventional crystal plasticity (CP-EVPFFT) is lower than the other ones given by MFDM-EVPFFT. Considering now the field statistics on the relative stress σ_{eq}/Σ_{eq}, it is observed that the distributions are sharper for lower grain sizes. For $\bar{d} = 0.25\mu m$, the stress values are quite high and are closer to the average stress which is strong. This trend is consistent with high stress hotspots (see Fig. 4). Conversely, the case $\bar{d} = 10\mu m$ exhibits a behavior closer to the one obtained from CP-EVPFFT with a large number of regions where stresses are much lower than the average stress Σ_{eq}, see Fig. 5(b).

The contour plots of the equivalent cumulated plastic strain ε^p_{eq} are reported on

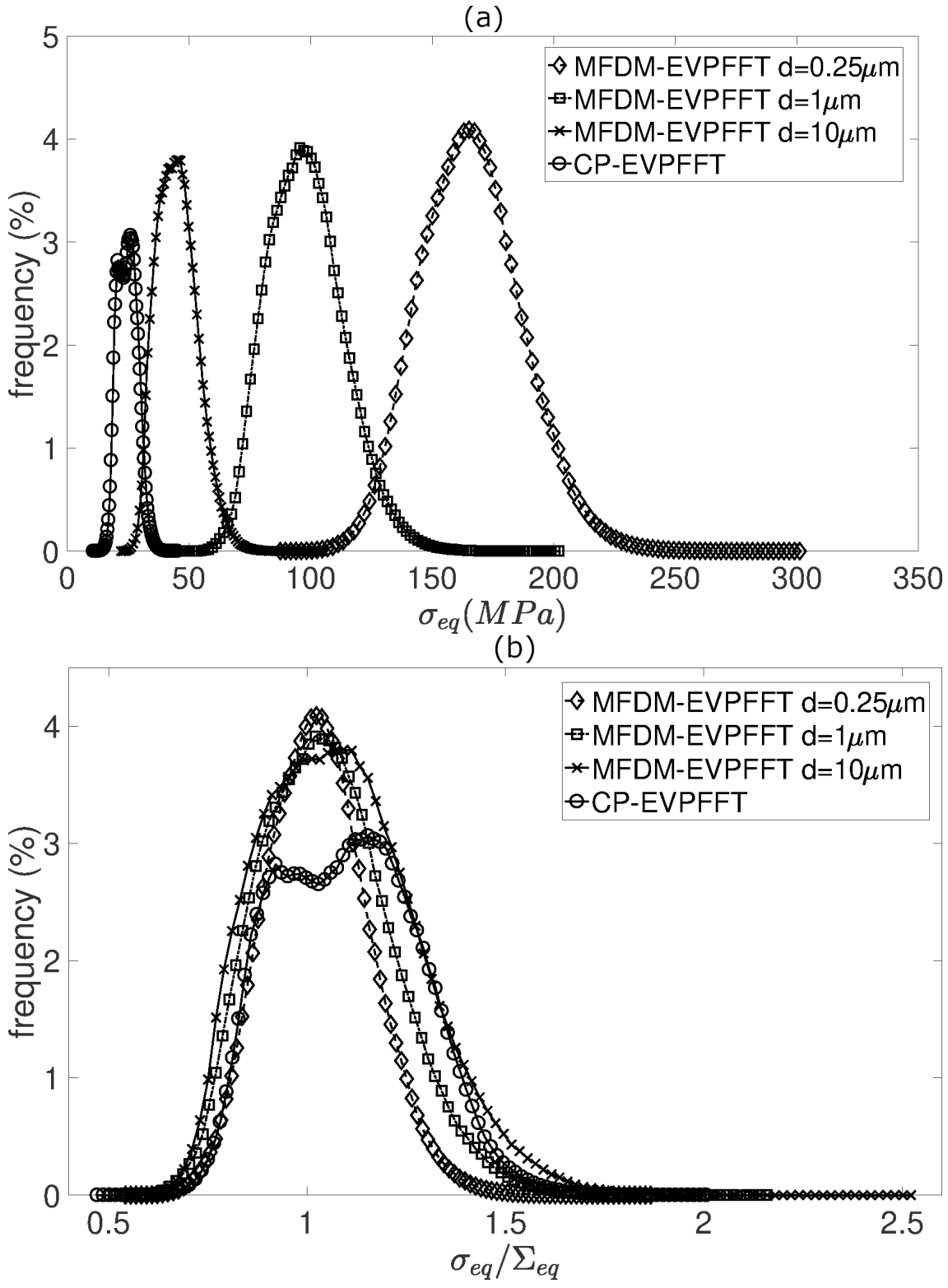

Figure 5. Histograms of σ_{eq} (a) and σ_{eq}/Σ_{eq} (b) recorded at $E^p_{33} = 0.2\%$ for different average grain sizes $\bar{d}$ with MFDM-EVPFFT and comparison with CP-EVPFFT.

Fig. 6(a-c) using MFDM-EVPFFT. For all grain sizes, it is seen that ε^p_{eq} is quite heterogeneous and deformation bands occur. A significant evolution of ε^p_{eq} is observed when $\bar{d}$ is decreasing from $10\mu m$ (Fig. 6(c)) to $0.25\mu m$ (Fig. 6(a)), where a network of strain localization bands occurs using MFDM-EVPFFT. At lower grain sizes, the regions where plastic strain cannot develop are larger inside grains due to stronger slip gradients. This explains why plastic strain described by ε^p_{eq} becomes more localized in deformation bands and stronger inside them for lowest grain size $\bar{d} = 0.25\mu m$. Conversely, Fig. 6(d) shows that plastic strain is more homogeneous in the case of CP-EVPFFT.

This is confirmed by the histograms reported on Fig. 7 using 100 bin values. For a same overall plastic strain ($E^p_{33} = 0.2\%$), higher peaks centered at smaller values of ε^p_{eq} are observed for small grain sizes, i.e. $\bar{d}$ lower than $1\mu m$. As shown in Fig. 7, the polycrystal with smallest grain size ($\bar{d} = 0.25\mu m$) exhibits a longer tail regarding the distribution of ε^p_{eq}. Therefore, for a same overall plastic strain, ε^p_{eq} is large in some regions corresponding to localized deformation bands crossing grains. Conversely, large grain sized polycrystals simulated with MFDM-EVPFFT or conventional plasticity simulated by CP-EVPFFT do no exhibit such long tails on the histograms of ε^p_{eq}, see Fig. 7. This corresponds to a more homogeneous plastic deformation distribution inside grains as given in Fig. 6(d).

The contour plots of ρ_{GND} expressed in m^{-2} obtained from the MFDM-EVPFFT model are reported on Fig. 8(a-c) for the three different grain sizes using the same scale range to study grain size effect on the spatial distributions of ρ_{GND}. These figures show that ρ_{GND} is increasing from grain interiors to grain boundaries and the magnitude of ρ_{GND} increases when $\bar{d}$ decreases. The ρ_{GND} field is high close to grain boundaries and spreads over the grain interiors. This is consistent with the assumption of a finite grain boundary affected zone used in internal length mean field

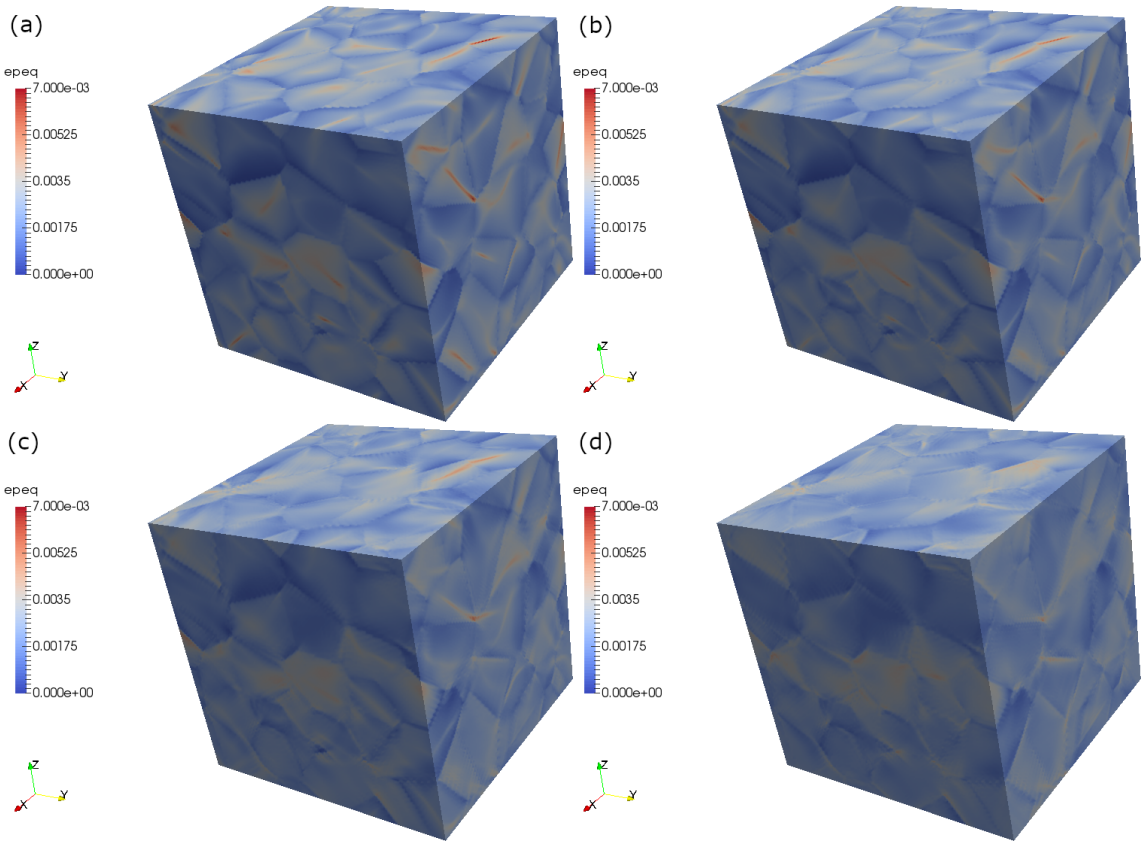

Figure 6. Spatial distribution of equivalent cumulated plastic strain ε_{eq}^{p} recorded at $E_{33}^{p} = 0.2\%$ for three average grain sizes $\bar{d}$ (MFDM-EVPFFT) with same scale range: $0.25\mu m$ (a), $1\mu m$ (b), $10\mu m$ (c). Simulation results with CP-EVPFFT (d) with same scale range.

approaches as developed by Pipard et al. (2009) for polycrystals with different mean grain sizes. The regions with high stress hotspots observed in Fig. 4(a) approximately correspond to high GND densities in Fig. 8(a), which means that important plastic strain incompatibility is present at these locations in the aggregate when grain size is smaller ($\bar{d} = 0.25\mu m$). For comparisons, the results obtained at $E_{33}^{p} = 0.2\%$ from the CP-EVPFFT model is reported on Fig. 8(d) for the ρ_{GND} field. This figure shows that in the case of conventional (local) plasticity, the calculated GND density is only localized at grain boundaries, i.e. only inter-granular GNDs. Indeed, there is no GND density pile up spreading inside the grain from grain boundaries and the magnitude of ρ_{GND} is much less important than in the case of the predictions given

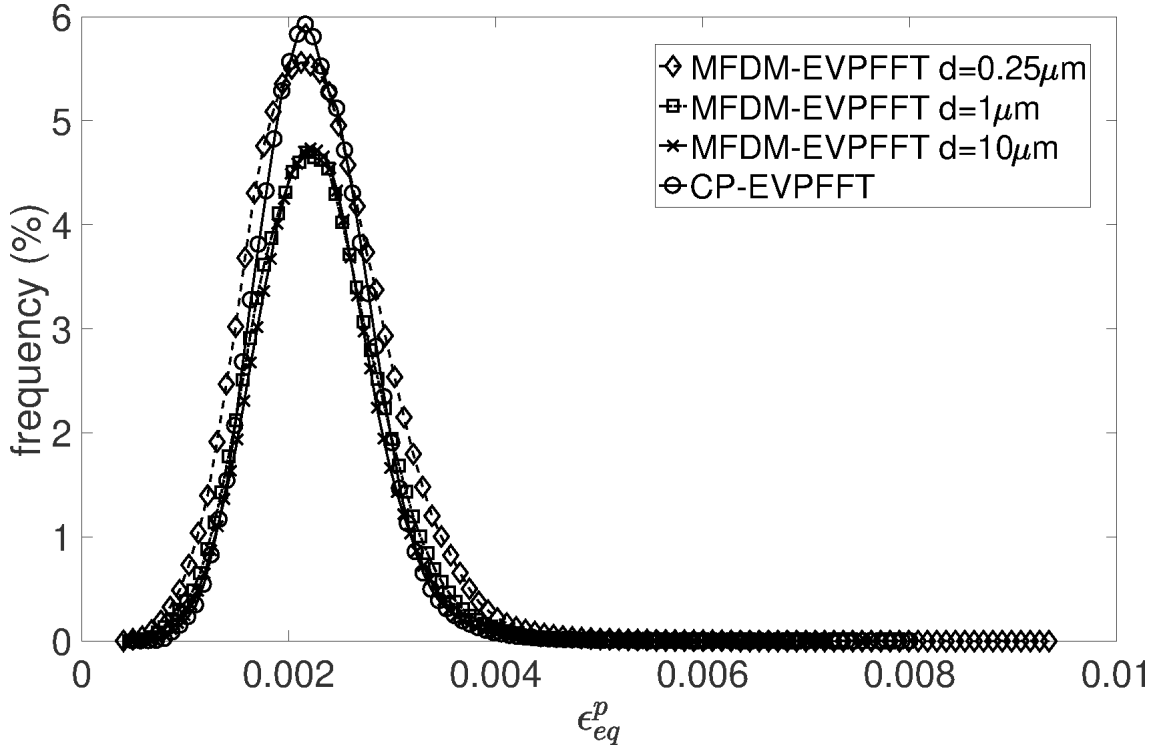

Figure 7. Histograms of ε^p_{eq} recorded at $E^p_{33} = 0.2\%$ for different average grain sizes $\bar{d}$ with MFDM-EVPFFT and comparison with CP-EVPFFT.

by the MFDM-EVPFFT model, see Fig. 8(d).

The histograms of $\alpha = \rho_{GND} b = \sqrt{\boldsymbol{\alpha} : \boldsymbol{\alpha}}$ expressed in mm^{-1} are reported on Fig. 9 (100 bin values). The histograms of α are strongly dependent on average grain size $\bar{d}$. Smaller grain-sized polycrystals, e.g. the MFDM-EVPFFT simulation with $\bar{d} = 0.25\mu m$, exhibit broader distribution peaks centered at larger values of α. Conversely, the histogram obtained with $\bar{d} = 10\mu m$ exhibits a high peak centered at a lower value of α. CP-EVPFFT demonstrates a very high distribution peak at very low values of α, which are approximately 3 order of magnitudes lower than the MFDM-EVPFFT simulations with $\bar{d} = 1\mu m$. In addition, conventional plasticity is responsible for a narrow distribution of α with too low values, which appear to be inconsistent at least qualitatively with GND profiles obtained from EBSD measurements for deformed polycrystals (Calcagnotto et al., 2010; Allain-Bonasso et al., 2012; Konijnenberg et al., 2015; Jiang et al., 2015; Wallis et al., 2016). Overall grain size effects (Hall-

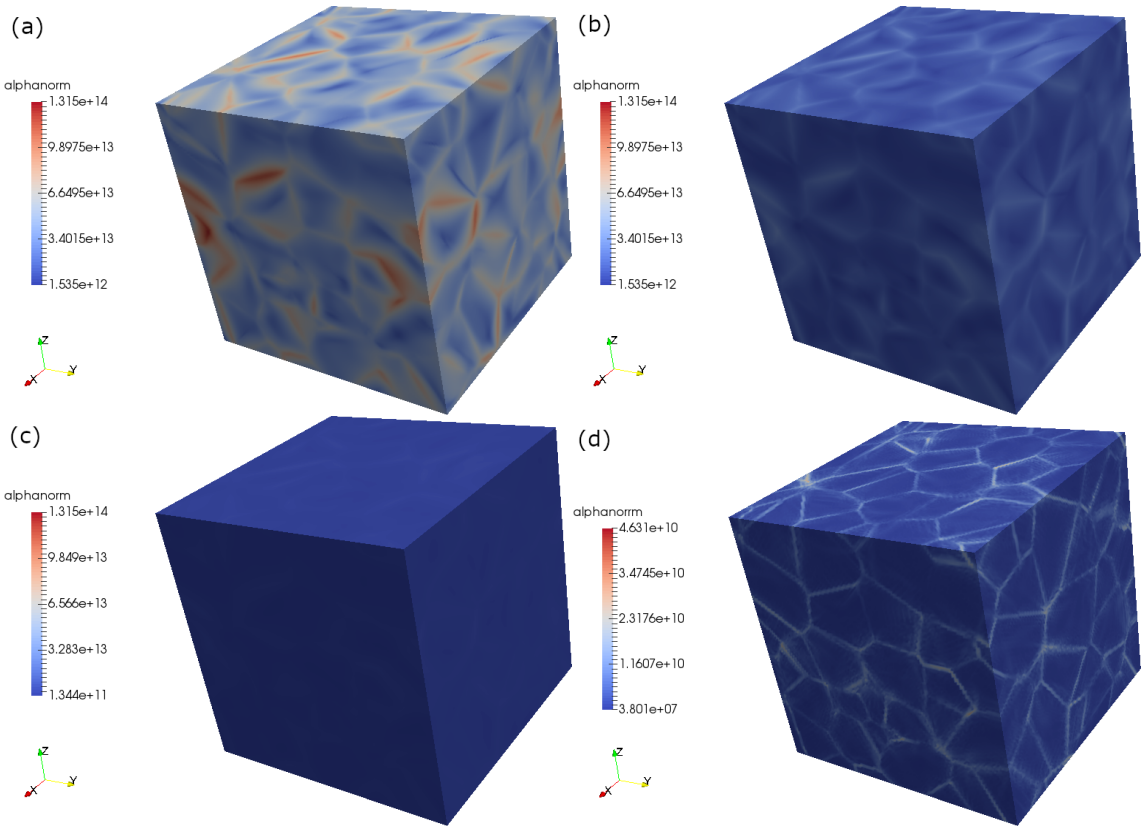

Figure 8. Spatial distribution of GND densities ρ_{GND} in m^{-2} recorded at $E^p_{33} = 0.2\%$ for three average grain sizes $\bar{d}$ (MFDM-EVPFFT) with same scale range: $0.25\mu m$ (a), $1\mu m$ (b), $10\mu m$ (c). Simulation results with CP-EVPFFT (d) with a different scale range.

Petch law) are due to the high level of GND densities for smaller grain sizes compared to larger ones and the spatial gradients of GND density. This is consistent with DDD results, where accumulation of geometrically necessary dislocations in the form of pile-ups is at the origin of the grain size effect of these microstructures (Lefebvre et al., 2007; Balint et al., 2010).

These numerical results demonstrate that a strong dependence on the grain size was observed on both cumulated plastic strain and on GND density in the course of a monotonous tensile test at low strains. However, even though stress hot spots obtained with MFDM-EVPFFT appears to be located where high GND densities are present (near grain boundaries or triple junctions), there is no clear spatial correlation between GND densities and cumulated plastic slip. Similar conclusions were ob-

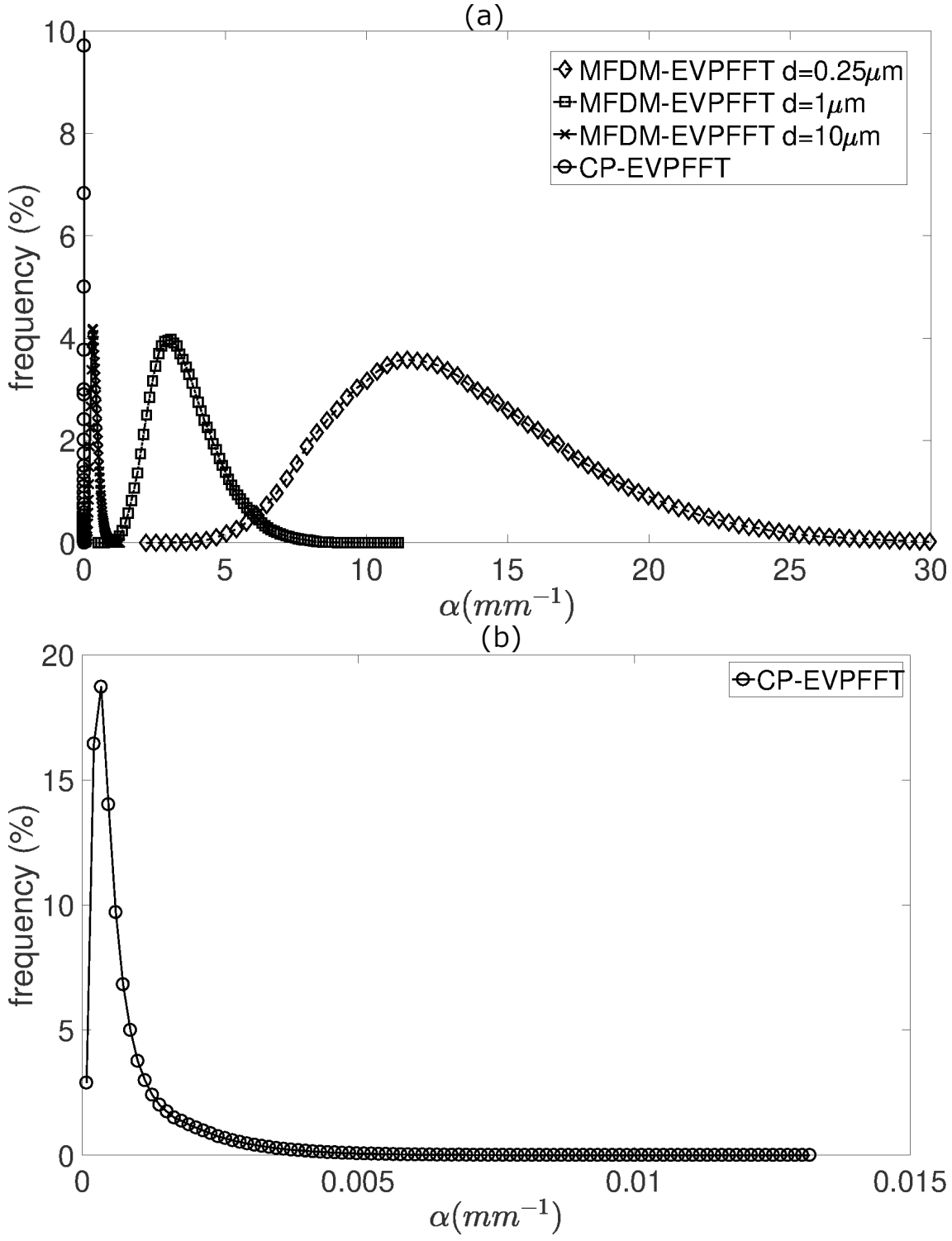

Figure 9. Histograms of GND densities ρ_{GND} recorded at $E^p_{33} = 0.2\%$ obtained with MFDM-EVPFFT at different grain sizes (a) and obtained with $CP - EVPFFT$ (zoom up) (b).

tained with the higher-order strain-gradient plasticity Gurtin's model (Gurtin, 2002) implemented in the EVPFFT formulation by Lebensohn and Needleman (2016) or in the case of the micromorphic approach developed for polycrystals by Cordero et al. (2012).

3.4 Reversible plasticity and Bauschinger effect

In addition to monotonic tensile loadings, tension-compression stress-strain responses and reversible plasticity are investigated using a RVE with $64 \times 64 \times 64$ voxels and 27 grains, see Fig. 1(b). Same materials parameters as before are used and comparisons are made between MFDM-EVPFFT and CP-EVPFFT to see the differences on the Bauschinger stress X. X is defined as the difference between the first stage tensile flow stress at $E_{33} = 0.2\%$ and the second stage compressive plastic flow stress at initial yielding in compression (deviation from the elastic slope at reversible loading). Then, the mechanical tests were stopped at $E_{33} = 0\%$ during compressive loading after forward tensile loading up to $E_{33} = 0.2\%$. Tension-compression responses simulated with MFDM-EVPFFT are reported on Fig. 10 for four mean grain sizes $\bar{d}$: $0.25\mu m$, $1.5472\mu m$, $15.472\mu m$ and $154.72\mu m$, respectively. These ones are also compared to the tension-compression responses given by the grain size independent CP-EVPFFT formulation. The Bauschinger stresses X are reported in Table 2 and show grain size dependence. X increases as $\bar{d}$ decreases following the predictions of MFDM-EVPFFT. The lowest Bauschinger stress is obtained with CP-EVPFFT and corresponds to classic inter-granular kinematic hardening with conventional crystal plasticity. This latter is a typical kinematic hardening which is classically present in bulk metals.

By specifically comparing the cyclic responses over a complete cycle: tension (up to $E_{33} = 0.2\%$) - compression (up to $E_{33} = -0.2\%$) - tension (up to $E_{33} = 0.2\%$)

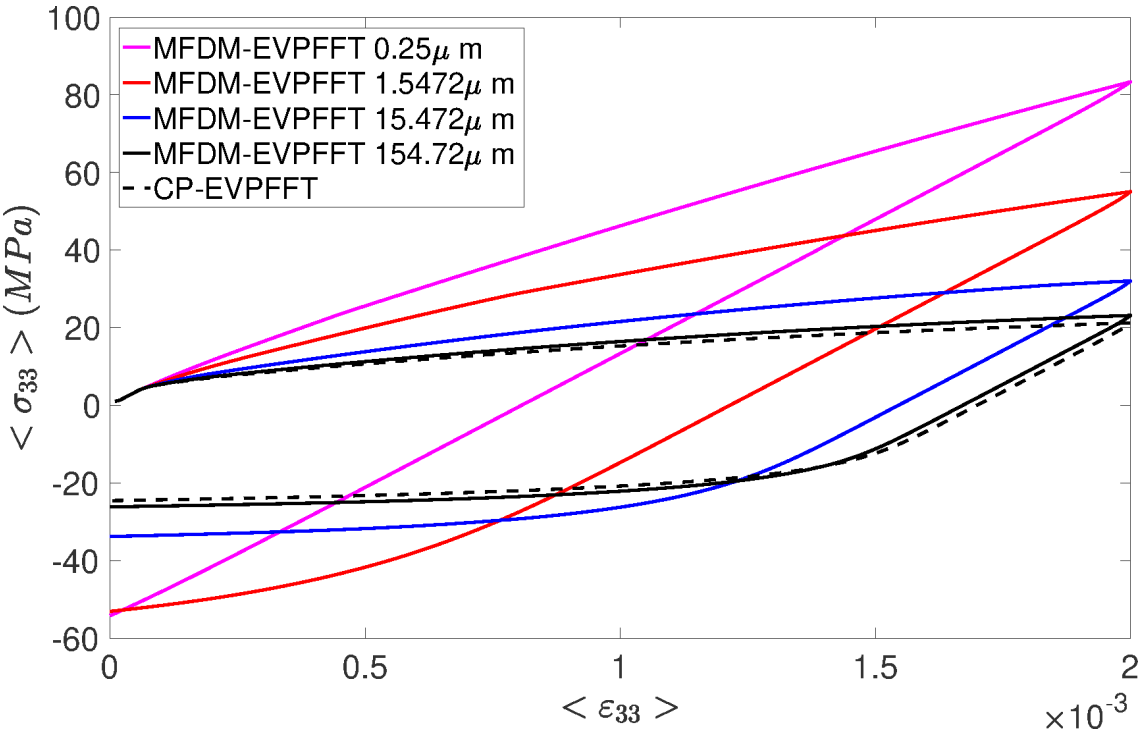

Figure 10. Reversible tension-compression tests performed with MFDM-EVPFFT (solid lines) for four average grain sizes $\bar{d}$: $0.25\mu m$, $1.5472\mu m$, $15.472\mu m$, $154.72\mu m$ and comparison with CP-EVPFFT (dotted line).

Table 2

Bauschinger stress X expressed in MPa for four simulations using MFDM-EVPFFT and CP-EVPFFT

CP-EVPFFT	MFDM-EVPFFT	MFDM-EVPFFT	MFDM-EVPFFT	MFDM-EVPFFT
size independent	$154.72\mu m$	$15.472\mu m$	$1.5472\mu m$	$0.25\mu m$
13.14	14.98	21.53	33.6	41.48

obtained from CP-EVPFFT and from MFDM-EVPFFT with $\bar{d} = 0.25\mu m$, it is observed on Fig. 11 that the MFDM-EVPFFT exhibits both stronger kinematic hardening at the origin of the Bauschinger stress X and stronger isotropic hardening as well. Therefore, it is interesting to study the evolution of both GND density and equivalent Von Mises stress from state A (resp. A') at the end of first tensile stage in Fig. 11, during the compression stage (states B (resp. B') and C (resp. C') on

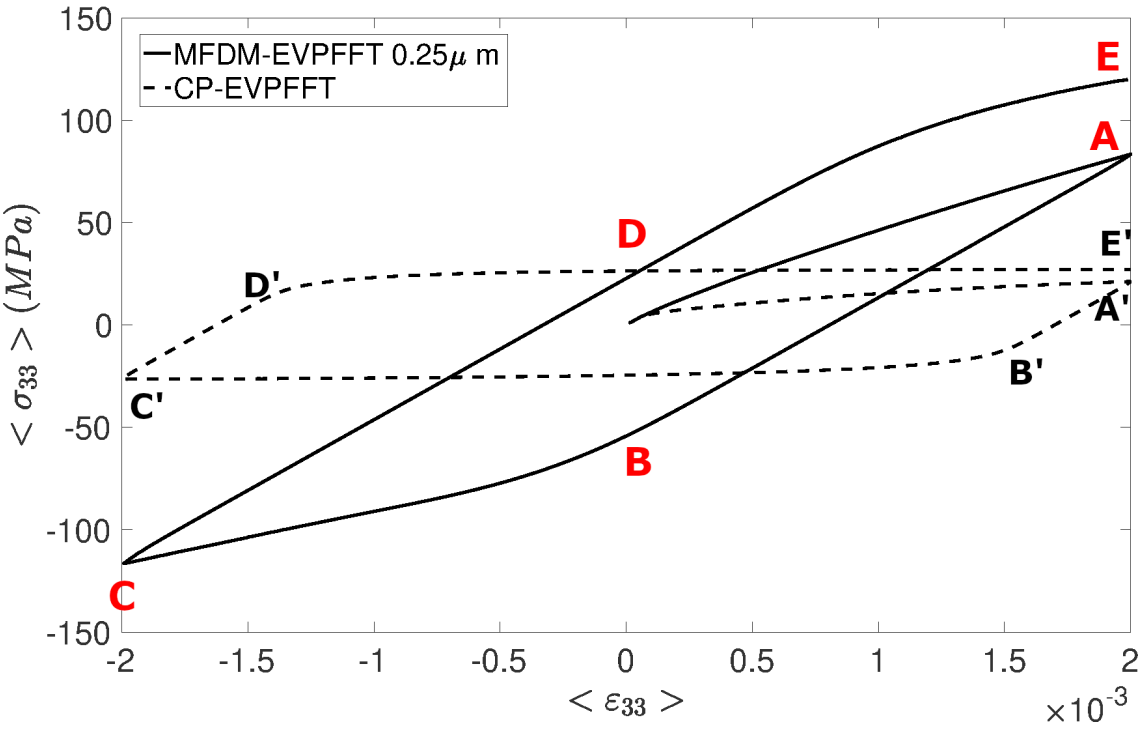

Figure 11. Tension-compression-tension cyclic tests performed with MFDM-EVPFFT (solid line) for $d = 0.25\mu m$ and with CP-EVPFFT (dotted line) for comparisons of the evolution of the macroscopic stress during cyclic loading. Different states A, B, C, D, E (resp. A', B', C', D', E') are marked on the figure using the MFDM-EVPFFT (resp. CP-EVPFFT) formulation.

Fig. 11) and during the second tensile stage (states D (resp. D') and E (resp. E') on Fig. 11). The notations A, B, C, D, E are used for the MFDM-EVPFFT simulation and A', B', C', D', E' are used for the CP-EVPFFT simulation.

As shown in Fig. 12, the evolution of ρ_{GND} from states A to E exhibits more important variations when calculated with the MFDM-EVPFFT model ($\bar{d} = 0.25\mu m$). In this figure, the reference scale for numerical values of ρ_{GND} in Fig. 12 is taken at state A, i.e. at the end of the first tensile stage. In between states A and B or states C and D, GND annihilations occur in the whole aggregate with lower levels of ρ_{GND} at states B and D. These dislocation annihilations are followed by GND density rebuilding up at states C and E. In conventional plasticity (CP-EVPFFT),

ρ_{GND} distributions are mainly located at the grain boundaries and exhibit some variations (essentially at states B' and D'), which are lower than the ones reported with MFDM-EVPFFT. This demonstrates that the Bauschinger stress found with CP-EVPFFT is mainly due to classic inter-granular stress accommodation as found by self-consistent models applied to metals, see e.g. Mareau and Berbenni (2015). With the MFDM-EVPFFT formulation, the development of internal stress during forward tensile loading, their relaxation and their re-building with inverse polarization during reverse loading is due to polarized dislocation microstructures formed in forward tensile loading, its annihilation and inverse polarization at reverse loading. This observation was also highlighted in different contributions using MFDM with the FE method for thin films (Roy and Acharya, 2006; Puri et al., 2011), composite materials (Richeton et al., 2011; Taupin et al., 2012) and ice single and multi-crystals (Taupin et al., 2007; Richeton et al., 2017). The corresponding evolutions of the stress field (σ_{eq}) for MFDM-EVPFFT ($\bar{d} = 0.25\mu m$) in comparison with CP-EVPFFT are reported for corresponding states A (resp. A') to E (resp. E') on Fig. 13. The reference scale for σ_{eq} in Fig. 13 is taken at state A (resp. A'). Like ρ_{GND}, stronger variations in magnitudes of σ_{eq} are observed using MFDM-EVPFFT compared to CP-EVPFFT.

Histograms of α (expressed in mm^{-1}) and uniaxial internal stress field measured by the quantity $\sigma_{33} - < \sigma_{33} >$ (expressed in MPa) for the 5 aforementioned states A (resp. A'), B (resp. B'), C (resp. C'), D (resp. D'), E (resp. E') allow to characterize the statistical description of plastic incompatibilities in the polycrystal during cyclic plasticity (here one cycle is considered). Figs. 14 and 15 both use 100 bin values and describe the spatial variations of α and $\sigma_{33} - < \sigma_{33} >$, respectively. Following Fig. 14, it is shown from that lattice incompatibility is partly removed at states B and D accompanied by a strong decrease of the stress field, see Fig. 13. Compared to reference state A, where the distribution peak of α is centered at $5mm^{-1}$, state

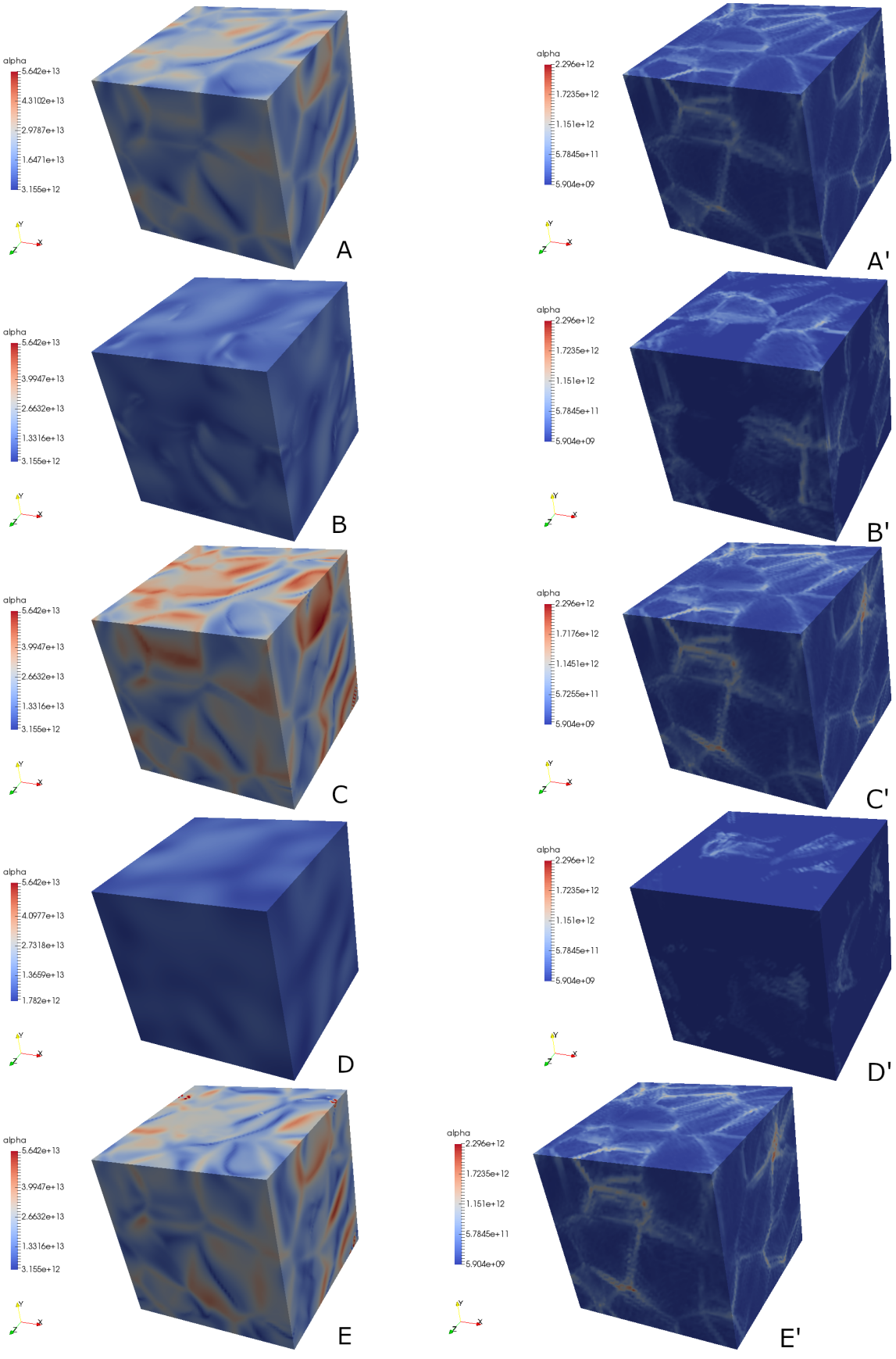

Figure 12. Evolution of GND density ρ_{GND} in m^{-2} during tension-compression-tension using present MFDM-EVPFFT (states A to E) with $\bar{d} = 0.25\mu m$ (left figures), using conventional CP-EVPFFT (states A' to E') (right figures).

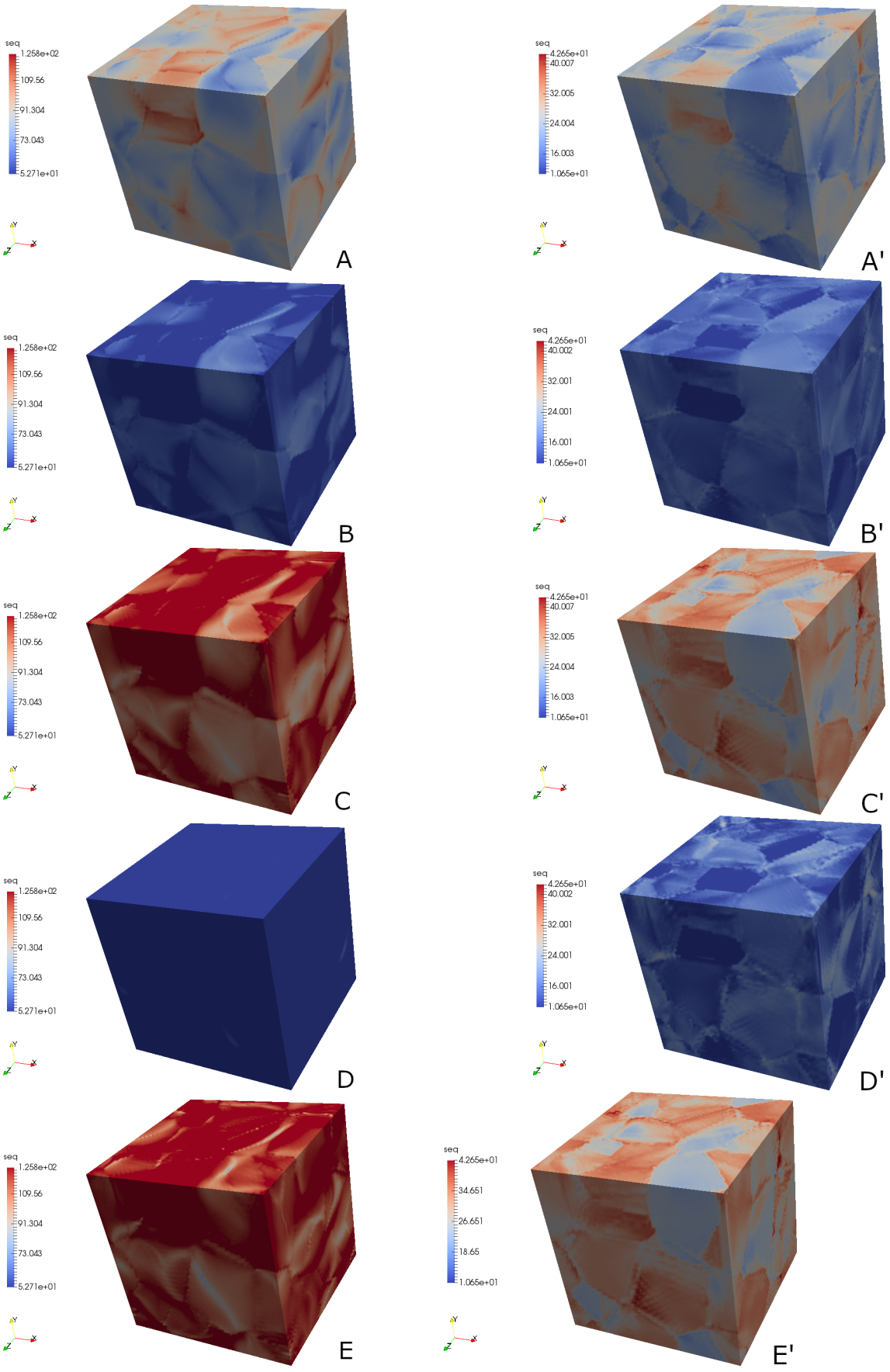

Figure 13. Evolution of σ_{eq} in MPa during tension-compression-tension using present MFDM-EVPFFT (states A to E) with $\bar{d} = 0.25\mu m$ (left figures), using conventional CP-EVPFFT (states A' to E') (right figures).

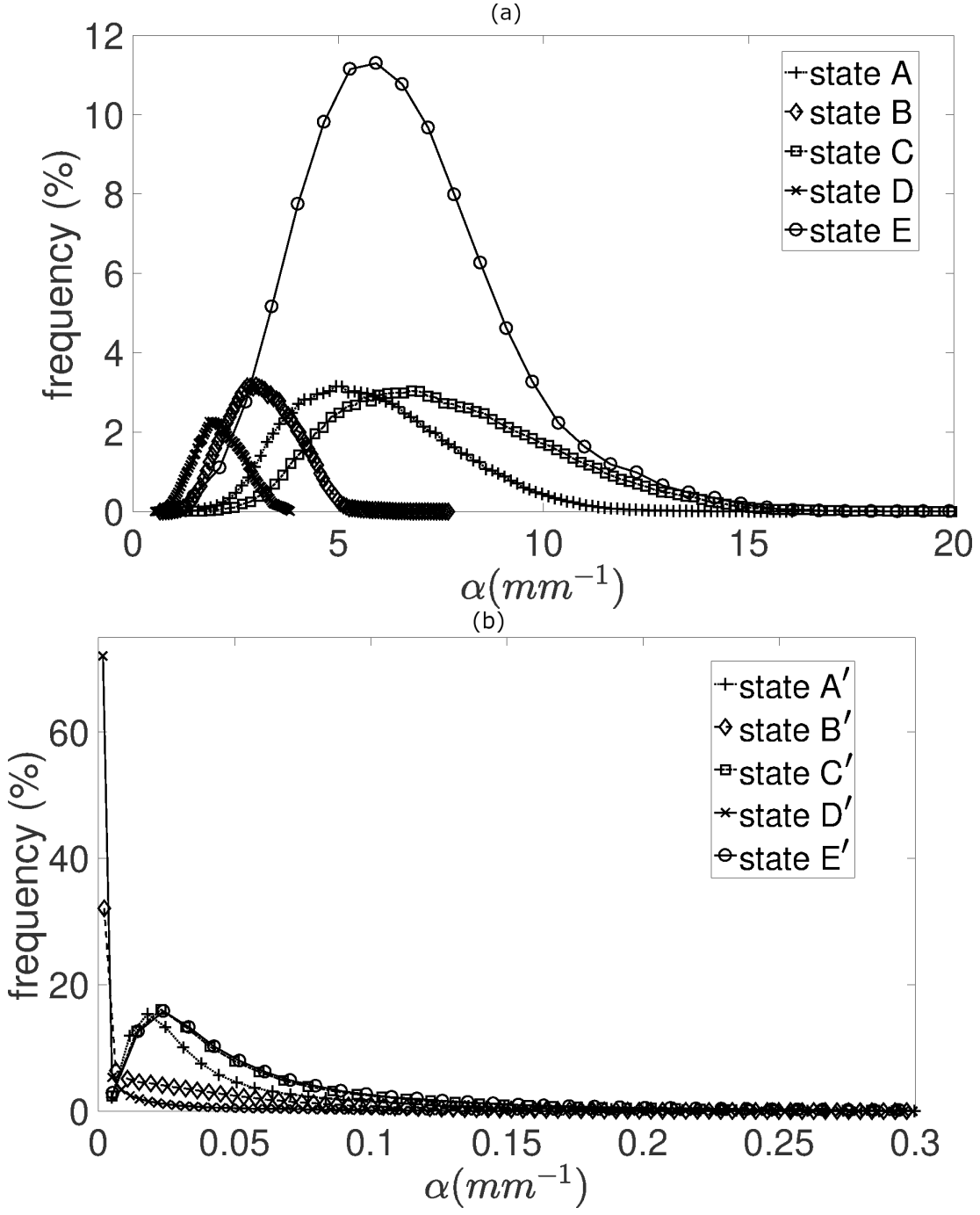

Figure 14. Histograms of the norm of the Nye tensor α (mm^{-1}) following the cycling loading simulated with MFDM-EVPFFT and recorded at the five states A, B, C, D, E (a), with CP-EVPFFT and recorded at the five states A', B', C', D', E' (b).

D exhibits the lowest values of α with a peak centered around $2mm^{-1}$ (at this state D, α is partly removed). At the end of state E, the highest values of α are found. In this state, the histogram shows a sharper peak around $6mm^{-1}$. Hence,

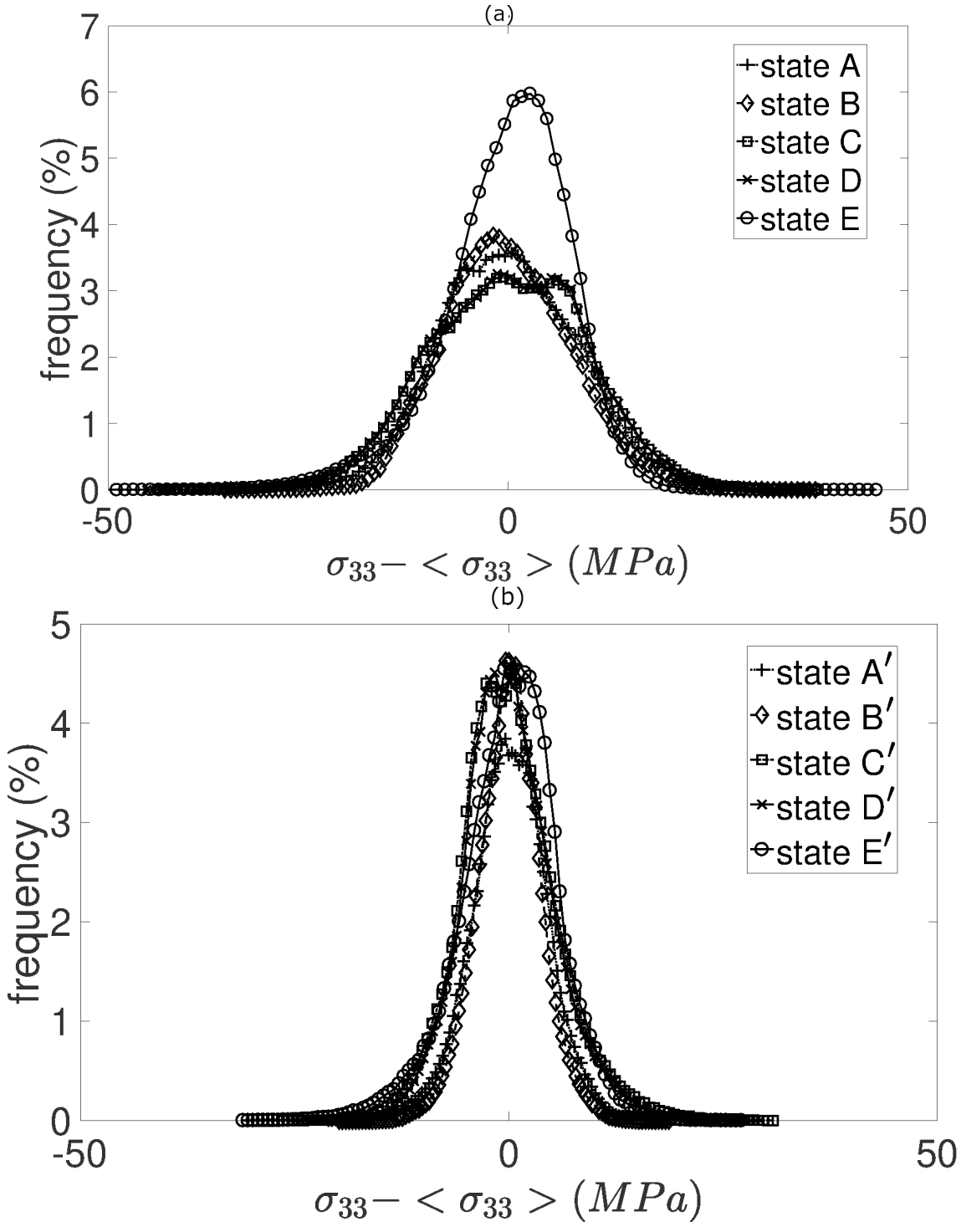

Figure 15. Histograms of internal stress field $\sigma_{33} - < \sigma_{33} >$ (MPa) following the cycling loading simulated with MFDM-EVPFFT and recorded at the five states A, B, C, D, E (a), with CP-EVPFFT and recorded at the five states A', B', C', D', E' (b).

the spatial variation of GND densities is more localized compared to previous states due to partial annihilation and rebuilding of GND density during the whole cycle. In comparison, the CP-EVPFFT simulations exhibit a decrease of GND densities at states B' and D' (in D' α takes the lowest values) and a small increase with a same distribution profile between A' and E', i.e. a strong peak centered around a low value of $\alpha = 0.02mm^{-1}$. Internal stress histograms (Fig. 15) first show that during the whole cycle the values of $\sigma_{33} - < \sigma_{33} >$ spread over a range of $-50MPa$ to $50MPa$ for MFDM-EVPFFT, while it is only around $-30MPa$ to $-30MPa$ for CP-EVPFFT. This explains the larger values of X observed with MFDM-EVPFFT compared to CP-EVPFFT, see Table 2. In the cases of states B and D, the histograms of $\sigma_{33} - < \sigma_{33} >$ obtained with MFDM-EVPFFT exhibits narrower distributions due to internal stress relaxation and GND density annihilations in these two intermediate states. A rebuilding of new larger internal stress state is obtained at the end of the cycle with a broader distribution at state E.

4 Conclusions

A spectral formulation called MFDM-EVPFFT was developed as an extension of the EVPFFT model (Lebensohn et al., 2012) that includes both GNDs and SSDs. The MFDM theory was earlier developed by Acharya and Roy (2006) and Roy and Acharya (2006) and implemented in finite elements to study small scale plasticity responses. The present FFT-based approach is able to efficiently account for average grain size effects on the flow stress of large 3D polycrystalline unit cells following a Hall-Petch law. Numerical simulations with different voxelized polycrystalline RVEs obtained with periodic Voronoi tessellations and different grain sizes were performed with $128 \times 128 \times 128$ voxels (100 grains) and $64 \times 64 \times 64$ voxels (27 grains). In this non local formulation including a spectral resolution of the space-time evolution of GND densities, the size dependence is related to the generation of higher GND density from grain interiors to grain boundaries as opposed to conventional crystal plasticity, which only describes low GND densities at grain boundaries. Statistical analyses with 100 bin histograms of mechanical fields show that GND density and equivalent plastic strains are not correlated. Higher GND densities are present in dislocation pile-ups from grain interior to grain boundaries and more localized accumulated slip in grain interior is observed for smaller grains sizes. These results extend to polycrystals the ones obtained by Djaka et al. (2019) for two-phase laminate microstructures. Besides, reversible plasticity is studied for polycrystals considering tension-compression-tension cycle. A grain size dependent Bauschinger translational strain-hardening is simulated for polycrystals with the MFDM-EVPFFT formulation.

Acknowledgements

S. Berbenni, V. Taupin thank the French State (ANR) through the program "Investment in the future" (LabEx "DAMAS" referenced as ANR-11-LABX-0008-01) for financial support. The work of R. A. Lebensohn was funded by Los Alamos National Laboratorys Laboratory-Directed Research and Development (LDRD) program.

References

Acharya, A., 2001. A model of crystal plasticity based on the theory of continuously distributed dislocations. Journal of the Mechanics and Physics of Solids 49, 761 – 784.

Acharya, A., 2003. Driving forces and boundary conditions in continuum dislocation mechanics. Proceedings of the Royal Society London A 459, 1343–1363.

Acharya, A., 2007. Jump condition for gnd evolution as a constraint on slip transmission at grain boundaries. Philosophical Magazine 87, 1349–1359.

Acharya, A., 2011. Microcanonical entropy and mesoscale dislocation mechanics and plasticity. Journal of Elasticity 104, 23–44.

Acharya, A., Bassani, J. L., 2000. Lattice incompatibility and a gradient theory of crystal plasticity. Journal of the Mechanics and Physics of Solids 48(8), 1565–1595.

Acharya, A., Beaudoin, A. J., 2000. Grain size effect in viscoplastic polycristals at moderate strains. Journal of the Mechanics and Physics of Solids 48, 2213 – 2230.

Acharya, A., Roy, A., 2006. Size effects and idealized dislocation microstructure at small scales : Predictions of a Phenomenological model of Mesoscopic Field Dislocation Mechanics : Part I. J. Mech. Phys. Solids 54, 1687–1710.

Acharya, A., Roy, A., Sawant, A., 2006. Continuum theory and methods for coarse-grained plasticity. Scripta Mater. 54, 705–710.

Allain-Bonasso, N., Wagner, F., Berbenni, S., Field, D. P., 2012. A study of the heterogeneity of plastic deformation in IF steel by EBSD. Materials Science Engineering A 548, 56–63.

Anglin, B. S., Lebensohn, R. A., Rollett, A. D., 2014. Validation of a numerical method based on fast Fourier transforms for heterogeneous thermoelastic materials by comparison with analytical solutions. Computational Materials Science 87, 209–217.

Armstrong, R., Douthwaite, I., Petch, N. J., 1962. The plastic deformation of polycrystalline aggregates. Philosophical Magazine 7, 45–58.

Arora, R., Acharya, A., 2019. Dislocation pattern formation in finite deformation crystal plasticity. International Journal of Solids and Structures, https://doi.org/10.1016/j.ijsolstr.2019.02.013, 2019.

Arsenlis, A., Parks, D. M., 1999. Crystallographic aspects of geometrically necessary and statistically stored dislocation density. Acta Mater. 47, 1597–1611.

Arsenlis, A., Parks, D. M., 2002. Modeling the evolution of crystallographic dislocation density in crystal plasticity. Journal of the Mechanics and Physics of Solids 50, 1979–2009.

Ashby, M. F., 1970. Deformation of plastically non-homogeneous materials. Philosophical Magazine 21, 399–424.

Balint, D. S., Deshpande, V. S., Needleman, A., Van der Giessen, E., 2010. Discrete dislocation plasticity analysis of the grain size dependence of the flow strength of polycrystals. International Journal of Plasticity 24, 2149–2172.

Barabash, R. I., Ice, G. E., Pang, J. W. L., 2005. Gradients of geometrically necessary dislocations from white beam microdiffraction. Materials Science Engineering A 400-401, 125–131.

Barbe, F., Decker, L., Jeulin, D., Cailletaud, G., 2001a. Intergranular and intragranular behavior of polycrystalline aggregates. Part I. F.E. model. International

Journal of Plasticity 17, 513–536.

Barbe, F., Forest, S., Cailletaud, G., 2001b. Intergranular and intragranular behavior of polycrystalline aggregates. Part II. Results. International Journal of Plasticity 17, 537–563.

Beausir, B., Fressengeas, C., Gurao, N. P., Toth, L. S., Suwas, S., 2009. Spatial correlation in grain misorientation distribution. Acta Materialia 57 (18), 5382–5395.

Berbenni, S., Berveiller, M., Richeton, T., 2008. Intra-granular plastic slip heterogeneities: Discrete vs. Mean Field approaches. International Journal of Solids and Structures 45, 4147–4172.

Berbenni, S., Favier, V., Berveiller, M., 2007. Impact of the grain size distribution on the yield stress of heterogeneous materials. International Journal of Plasticity 23, 114–142.

Berbenni, S., Taupin, V., 2018. Fast Fourier Transform-based micromechanics of interfacial line defects in crystalline materials. Journal of Micromechanics and Molecular Physics 1840007, doi:10.1142/S2424913018400076.

Berbenni, S., Taupin, V., Djaka, K. S., Fressengeas, C., 2014. A numerical spectral approach for solving elasto-static field dislocation and g-disclination mechanics. International Journal of Solids and Structures 51, 4157–4175.

Berbenni, S., Taupin, V., Fressengeas, C., Capolungo, L., 2016. A fast Fourier transform-based approach for generalized disclination mechanics within a couple stress theory. Generalized Continua as Models for Classical and Advanced Materials, Advanced Structured Materials,H. Altenbach and S. Forest (eds.), Springer International Publishing Switzerland, 47–75.

Bertin, N., Capolungo, L., 2018. A FFT-based formulation for discrete dislocation dynamics in heterogeneous media. Journal of Computational Physics 355, 366–384.

Bertin, N., Upadhyay, M. V., Pradalier, C., Capolungo, L., 2015. A FFT-based formulation for efficient mechanical fields computation in isotropic and anisotropic periodic discrete dislocation dynamics. Modelling and Simulation in Materials Science and Engineering 23, 065009.

Berveiller, M., 1978. Contribution à l'étude du comportement plastique des textures de déformation des polycristaux métalliques. Thèse d'Etat de l'Université Paris 13.

Berveiller, M., Zaoui, A., 1979. An extension of the self-consistent scheme to plastically-flowing polycrystals. Journal of the Mechanics and Physics of Solids 26, 325–344.

Biner, S. B., Morris, J. R., 2002. A two-dimensional discrete dislocation simulation of the effect of grain size on strengthening behaviour. Modelling and Simulation in Materials Science and Engineering 10 (6), 617–635.

Brenner, R., Beaudoin, A. J., Suquet, P., Acharya, A., 2014. Numerical implementation of static Field Dislocation Mechanics theory for periodic media. Philosophical Magazine, 1–24.

Brenner, R., Lebensohn, R. A., Castelnau, O., 2009. Elastic anisotropy and yield surface estimates of polycrystals. International Journal of Solids and Structures 46, 3018–3026.

Budiansky, B., Wu, T. T., 1962. Theoretical prediction of plastic strains of polycrystals. Proceedings of the 4th US National Congress of Applied Mechanics. Transactions of AIME, 1175–1185.

Busso, E. P., Meisonnier, F. T., O'Dowd, N. P., 2000. Gradient-dependent deformation of two-phase single crystals. Journal of the Mechanics and Physics of Solids 48, 2333–2361.

Calcagnotto, M., Ponge, D., Demir, E., Raabe, D., 2010. Orientation gradients and geometrically necessary dislocations in ultrafine grained dual-phase steels studied

by 2D and 3D EBSD. Materials Science Engineering A 527, 2738–2746.

Cheong, K. S., Busso, E. P., Arsenlis, A., 2005. A study of microstructural length scale effects on the behaviour of FCC polycrystals using strain gradient concepts. International Journal of Plasticity 21, 1797–1814.

Collard, C., Favier, V., Berbenni, S., Berveiller, M., 2010. Role of discrete intragranular slip bands on the strain-hardening of polycrystals. International Journal of Plasticity 26, 310–328.

Cordero, N. M., Forest, S., Busso, E. P., Berbenni, S., Cherkaoui, M., 2012. Grain size effects on plastic strain and dislocation density tensor fields in metal polycrystals. Computational Materials Science 52, 7–13.

Cordero, N. M., Gaubert, A., Forest, S., Busso, E. P., Galerneau, F., Kruch, S., 2010. Size effects in generalised continuum crystal plasticity for two-phase laminates. Journal of the Mechanics and Physics of Solids 58, 1963–1994.

Cordero, Z. C., Knight, B. E., Schuh, C. A., 2016. Six decades of the Hall-Petch effect: a survey of grain size strengthening studies on pure metals. International Materials Reviews 61 (8), 495–512.

Delaire, F., Raphanel, J. L., Rey, C., 2000. Plastic heterogeneities of a copper multicrystal deformed in uniaxial tension: experimental study and finite element simulations. Acta Materialia 48, 1075–1087.

Djaka, K. S., Berbenni, S., Taupin, V., Lebensohn, R. A., 2019. A FFT-based numerical implementation of mesoscale field dislocation mechanics: application to two-phase laminates. International Journal of Solids and Structures, https://doi.org/10.1016/j.ijsolstr.2018.12.027, 2019.

Djaka, K. S., Taupin, V., Berbenni, S., Fressengeas, C., 2015. A numerical spectral approach to solve the dislocation density transport equation. Modelling and Simulation in Materials Science and Engineering 23, 065008(27pp).

Djaka, K. S., Villani, A., Taupin, V., Capolungo, L., Berbenni, S., 2017. Field disloca-

tion mechanics for heterogeneous elastic materials: A numerical spectral approach. Computer Methods in Applied Mechanics and Engineering 315, 921–942.

Donegan, S. P., Rollett, A. D., 2015. Simulation of residual stress and elastic energy density in thermal barrier coatings using fast Fourier transforms. Acta Materialia 96, 212–228.

Dreyer, W., Müller, W. H., Olschewski, J., 1999. An approximate analytical 2D-solution for the stresses and strains in eigenstrained cubic materials. Acta Mech. 136 (3-4), 171–192.

Eisenlohr, P., Diehl, M., Lebensohn, R. A., Roters, F., 2013. A spectral method solution to crystal elasto-viscoplasticity at finite strains. Int. J. Plast. 46, 37–53.

El-Naaman, S. A., Nielsen, K. L., Niordson, C. F., 2019. An investigation of back stress formulations under cyclic loading. Mechanics of Materials 130, 76–87.

Eloh, K. S., Jacques, A., Berbenni, S., 2019. Development of a new consistent discrete Green operator for FFT-based methods to solve heterogeneous problems with eigenstrains. International Journal of Plasticity 116, 1–23.

Espinosa, H., Berbenni, S., Panico, M., Schwarz, K., 2005. An interpretation of size scale plasticity in geometrically confined systems. Proceedings of the National Academy of Sciences USA 102 (47), 16933–16938.

Espinosa, H., Panico, M., Berbenni, S., Schwarz, K., 2006. Discrete dislocation dynamics simulations to interpret plasticity size and surface effects in freestanding FCC thin films. International Journal of Plasticity 22 (11), 2091–2117.

Evers, L. P., Brekelmans, W. A. M., Geers, M. G. D., 2004. Non-local crystal plasticity model with intrinsic SSD and GND effects. Journal of the Mechanics and Physics of Solids 52, 2379–2401.

Evers, L. P., Parks, D. M., Brekelmans, W. A. M., Geers, M. G. D., 2002. Crystal plasticity model with enhanced hardening by geometrically necessary dislocation accumulation. Journal of the Mechanics and Physics of Solids 50, 2403–2424.

Eyre, D. J., Milton, G. W., 1999. A fast numerical scheme for computing the response of composite using grid refinement. European Physical Journal - Applied Physics 6, 41–47.

Fleck, N. A., Hutchinson, J. W., 1993. A phenomenological theory of strain gradient plasticity. J. Mech. Phys. Solids 41, 1825–1857.

Fleck, N. A., Hutchinson, J. W., 2001. Reformulation of strain gradient plasticity. Journal of the Mechanics and Physics of Solids 48, 2245–2271.

Fleck, N. A., Hutchinson, J. W., Willis, J. R., 2015. Guidelines for constructing strain gradient plasticity theories. Trans. ASME Journal of Applied Mechanics 82, 071002–10pages.

Fleck, N. A., Willis, J. R., 2009. A mathematical basis for strain-gradient plasticity theory- Part I: scalar plastic multiplier. Journal of the Mechanics and Physics of Solids 57, 161–177.

Graham, J. T., Rollett, A. D., LeSar, R., 2016. Fast fourier transform discrete dislocation dynamics. Modell. Simul. Mater. Sci. Eng. 8, 085005.

Grennerat, F., Montagnat, M., Castelnau, O., Vacher, P., Moulinec, H., Suquet, P., Duval, P., 2012. Experimental characterization of the intragranular strain field in columnar ice during transient creep. Acta Mater. 60, 3655–3666.

Gudmundson, P., 2004. A unified treatment of strain gradient plasticity. Journal of the Mechanics and Physics of Solids 52, 1379–1406.

Gupta, S., Beaudoin, A. J., Chevy, J., 2017. Strain rate jump induced negative strain rate sensitivity (nsrs) in aluminium alloy 2024: Experiments and constitutive modeling. Materials Science Engineering A 683, 143–152.

Gurtin, M., 2002. A gradient theory of single-crystal viscoplasticity that accounts for geometrically necessary dislocations. Journal of the Mechanics and Physics of Solids 50, 5–32.

Gurtin, M. E., Anand, L., 2009. Thermodynamics applied to gradient theories involv-

ing accumulated plastic strain: The theories of Aifantis and Fleck and Hutchinson and their generalization. Journal of the Mechanics and Physics of Solids 57, 405–421.

Gurtin, M. E., Anand, L., Lele, S. P., 2007. Gradient single-crystal plasticity with free energy dependent on dislocation densities. Journal of the Mechanics and Physics of Solids 55, 1853–1878.

Guruprasad, P. J., Carter, W. J., Benzerga, A. A., 2008. A discrete dislocation analysis of the Bauschinger effect in microcrystals. Acta Materialia 56, 5477–5491.

Hall, E. O., 1951. The deformation and ageing of mild steels. Proc. Phys. Soc. London B 64, 747–753.

Han, C. S., Gao, H., Huang, Y., Nix, W. D., 2005. Mechanism-based strain gradient crystal plasticity-i. theory. Journal of the Mechanics and Physics of Solids 53, 1188–1203.

Hansen, N., 1985. Polycrystalline strengthening. Metallurgical Transactions A 16A, 2167.

Hansen, N., 2004. Hall-Petch relation and boundary strengthening. Scripta Materialia 51, 801–806.

Haouala, S., Lucarini, S., Llorca, J., Segurado, J., 2020. Simulation of the Hall-Petch effect in FCC polycrystals by means of strain gradient crystal plasticity and FFT homogenization. Journal of the Mechanics and Physics of Solids 134, 103755.

Hill, R., 1965. Continuum micromechanics of elastoplastic polycrystals. Journal of the Mechanics and Physics of Solids 13, 89–101.

Hirth, J. P., 1972. The influence of grain boundaries on mechanical properties. Metallurgical Transactions 3, 3047–3067.

Jiang, J., Britton, T. B., Wilkinson, A. J., 2015. Evolution of intragranular stresses and dislocation densities during cyclic deformation of polycrystalline copper. Acta Materialia 94, 193–204.

Jiang, M., Devincre, B., Monnet, G., 2019. Effects of the grain size and shape on the flow stress: A dislocation dynamics study. International Journal of Plasticity 113, 111–124.

Kabel, M., Fliegener, S., Schneider, M., 2016. Mixed boundary conditions for FFT-based homogenization at finite strains. Comp. Mech. 57 (2), 193–210.

Kiener, D., Motz, C., Grosinger, W., Weygand, D., Pippan, R., 2010. Cyclic response of copper single crystal micro-beams. Scripta Materialia 63, 500–503.

Konijnenberg, P. J., Zaefferer, S., Raabe, D., 2015. Assessment of geometrically necessary dislocation levels derived by 3D EBSD. Acta Materialia 99, 402–414.

Kröner, E., 1958. Kontinuumstheorie der Versetzungen und Eigenspannungen. Collatz L and Loesch F (eds.). Ergebnisse der Angewewandte Mathematik 5, Springer Verlag, Berlin.

Kröner, E., 1961. Zur plastischen Verformung des Vielkristalls. Acta Metallurgica 9, 155–161.

Kröner, E., 1981. Continuum theory of defects. In: Balian R et al (Eds) Physics of defects Les Houches Session 35 North Holland, New York, 215–315.

Kubin, L. P., Canova, G., Condat, M., Devincre, B., Pontikis, V., Bréchet, Y., 1992. Dislocation microstructure and plastic flow : a 3-d simulation. Solid state Phenomena 23-24, 455–472.

Lavergne, F., Brenner, R., Sab, K., 2013. Effects of grain size distribution on the stress heterogeneity on yield stress of polycrystals. Computational Materials Science 77, 387–398.

Lebensohn, R., 2001. N-site modeling of a 3D viscoplatic polycrystal using Fast Fourier Transform. Acta Materialia 49, 2723–2737.

Lebensohn, R., Brenner, R., Castelnau, O., Rollett, A., 2008. Orientation image-based micromechanical modelling of subgrain texture evolution in polycrystalline copper. Acta Mater. 56, 3914–3926.

Lebensohn, R., Escobedo, J., Cerreta, E., Dennis-Koller, D., Bronkhorst, C., Bingert, J., 2013. Modeling void growth in polycrystalline materials. Acta Mater. 61, 6918–6932.

Lebensohn, R., Montagnat, M., Mansuy, P., Duval, P., Meysonnier, J., Philip, A., 2009. Modeling viscoplastic behavior and heterogeneous intracrystalline deformation of columnar ice polycrystals. Acta Mater. 57, 1405–1415.

Lebensohn, R. A., Castelnau, O., Brenner, R., Gilormini, P., 2005. Study of the antiplane deformation of linear 2-D polycrystals with different microstructures. International Journal of Solids and Structures 46, 3018–3026.

Lebensohn, R. A., Idiart, M. I., Ponte-Castañeda, Vincent, P. G., 2011. Dilatational viscoplasticity of polycrystalline solids with intergranular cavities. Philosophical Magazine 91, 3038–3067.

Lebensohn, R. A., Kanjarla, A. K., Eisenlohr, P., 2012. An elasto-viscoplastic formulation based on Fast Fourier Transforms for the prediction of micromechanical fields in polycrystalline materials. International Journal of Plasticity 32-33, 59–69.

Lebensohn, R. A., Needleman, A., 2016. Numerical implementation of non-local polycrystal plasticity using fast Fourier transforms. J. Mech. Phys. Solids 97, 333–351.

Lebensohn, R. A., Tomé, C. N., 1993. A self-consistent anisotropic approach for the simulation of plastic deformation and texture development of polycrystals. Acta Metallurgica and Materialia 41, 2611–2624.

Lee, S. B., Lebensohn, R. A., Rollett, A. D., 2011. Modeling the viscoplastic micromechanical response of two-phase materials using Fast Fourier Transforms. International Journal of Plasticity 27, 707–727.

Lefebvre, S., Devincre, B., Hoc, T., 2007. Yield stress strengthening in ultrafine-grained metals: A two-dimensional simulation of dislocation dynamics. Journal of the Mechanics and Physics of Solids 55, 788–802.

Li, J., Tian, X. X., Abdelmoula, R., 2012. A damage model for crack prediction in brittle and quasi-brittle materials solved by the FFT method. International Journal of Fracture 173, 135–146.

Lucarini, S., Segurado, J., 2019. On the accuracy of spectral solvers for micromechanics based fatigue modeling. Computational Mechanics 63, 365–382.

Mareau, C., Berbenni, S., 2015. An affine formulation for the self-consistent modeling of elasto-viscoplastic heterogeneous materials based on the translated field method. International Journal of Plasticity 64, 134–150.

Mareau, C., Daymond, M. R., 2016. Micromechanical modelling of twinning in polycrystalline materials: Application to magnesium. International Journal of Plasticity 85, 156–171.

Masson, R., Bornert, M., Suquet, P., Zaoui, A., 2000. An affine formulation for the prediction of the effective properties of non linear composites and poly-crystals. Journal of the Mechanics and Physics of Solids 48 (6-7), 1203–1227.

Mecking, H., 1981. Low-temperature deformation of polycrystals. In: Deformation of polycrystals. N. Hansen et al. (eds). Riso National laboratory, Roskilde, Denmark, pp. 73–86.

Mecking, H., Kocks, U. F., 1981. Kinetics of flow and strain-hardening. Acta Metallurgica 29, 1865–1875.

Mercier, S., Molinari, A., 2009. Homogenization of elasticviscoplastic heterogeneous materials: self-consistent and Mori-Tanaka schemes. International Journal of Plasticity 25, 1024–1048.

Meyers, M. A., Chawla, K. K., 1984. Grain size strengthening (chapter 14). In: Mechanical Metallurgy: Principles and Applications. Prentice-Hall, Englewood Cliffs, New Jersey, pp. 494–514.

Michel, J. C., Moulinec, H., Suquet, P., 2001. A computational scheme for linear and non-linear composites with arbitrary phase contrast. International Journal of

Numerical Methods Engineering 52, 139–160.

Mika, D. P., Dawson, P. R., 1998. Effects of grain interaction on deformation in polycrystals. Mater Sci Eng A 257, 62–76.

Molinari, A., Canova, G. R., Ahzi, S., 1987. A self-consistent approach of the large deformation polycrystal viscoplasticity. Acta Metallurgica and Materialia 35, 2983–2994.

Moulinec, H., Suquet, P., 1994. A fast numerical method for computing the linear and non linear properties of composites. Comptes Rendus de l'Académie des Sciences de Paris II 318, 1417–1423.

Moulinec, H., Suquet, P., 1998. A numerical method for computing the overall response of nonlinear composites with complex microstructure. Comput. Meth. Appl. Mech. Eng. 157, 69–94.

Müller, W., 1996. Mathematical vs. experimental stress analysis of inhomogeneities in solids. Journal of Physics IV 6 (C1), 139–148.

Müller, W., 1998. Fourier transforms and their application to the formation of texture and changes of morphology in solids, in: iutam Edition. Kluwer Academic Publishers.

Nicola, L., Xiang, Y., Vlassak, J., VanderGiessen, E., Needleman, A., 2006. Plastic deformation of freestanding thin films: experiments and modeling. Journal of the Mechanics and Physics of Solids 54, 2089–2110.

Niordson, C., Hutchinson, J. W., 2003. Non-uniform plastic deformation of micron scale objects. International Journal for Numerical Methods in Engineering 56, 961–975.

Niordson, C. F., Kysar, J. W., 2014. Computational strain gradient crystal plasticity. Journal of the Mechanics and Physics of Solids 62, 31–47.

Niordson, C. F., Legarth, B. N., 2010. Strain gradient effects on cyclic plasticity. Journal of the Mechanics and Physics of Solids 58, 542–557.

Nye, J. F., 1953. Some geometrical relations in dislocated crystals. Acta Materialia 1, 153–162.

Ohno, N., Okumura, D., 2007. Higher-order stress and grain size effects due to self-energy of geometrically dislocations. Journal of the Mechanics and Physics of Solids 55, 1879–1898.

Ohno, N., Okumura, D., Shibata, T., 2008. Grain size dependent yield behavior under loading, unloading and reverse loading. International Journal of Modern Physics B 22, 5937–5942.

Otsuka, T., Brenner, R., Bacroix, B., 2018. FFT-based modelling of transformation plasticity in polycrystalline materials during diffusive phase transformation. International Journal of Engineering Sciences 127, 92–113.

Pantleon, W., 2008. Resolving the geometrically necessary dislocation content by conventional electron backscattering diffraction. Scripta Materialia 58 (11), 994–997.

Paramatmuni, C., Kanjarla, A. K., 2019. A crystal plasticity FFT based study of deformation twinning, anisotropy and micromechanics in HCP materials: Application to AZ31 alloy. International Journal of Plasticity 113, 269–290.

Peach, M., Koehler, J., 1950. The forces exerted on dislocations and the stress fields produced by them. Physical Review 80 (3), 436–439.

Perrin, C., Berbenni, S., Vehoff, H., Berveiller, M., 2010. Role of discrete intragranular slip on lattice rotations in polycrystalline Ni: Experimental and micromechanical studies. Acta Materialia 58, 4639–4649.

Petch, N. J., 1953. The cleavage strength of polycryystals. J. Iron Steel Inst. 174, 25–28.

Pipard, J. M., Nicaise, N., Berbenni, S., Bouaziz, O., Berveiller, M., 2009. A new mean field micromechanical approach to capture grain size effects. Computational Materials Science 45, 604–610.

Puri, S., Das, A., Acharya, A., 2011. Mechanical response of multicrystalline thin films in mesoscale field dislocation mechanics. Journal of the Mechanics and Physics of Solids 59, 2400–2417.

Puri, S., Roy, A., 2012. Plastic deformation of multicrystalline thin films: Grain size distribution vs. grain orientation. Computational Materials Science 52, 20–24.

Puri, S., Roy, A., Acharya, A., Dimiduk, D., 2009. Modeling dislocation sources and size effects at initial yield in continuum plasticity. Journal of Mechanics of Materials and Structures 4 (9), 1603–1618.

Randle, V., Hansen, N., Jensen, D. J., 1996. The deformation behaviour of grain boundary regions in polycrystalline aluminium. Philosophical Magazine A 73 (2), 265–282.

Richards, A. W., Lebensohn, R. A., Bhattacharya, K., 2013. Interplay of martensitic phase transformation and plastic slip in polycrystals. Acta Materialia 61, 4384–4397.

Richeton, T., Berbenni, S., Berveiller, M., 2009. Grain-size dependent accommodation due to intragranular distribution of dislocation loops. Acta Materialia 57, 1347–1356.

Richeton, T., Le, L. T., Chauve, T., Bernacki, M., Berbenni, S., Montagnat, M., 2017. Modelling the transport of geometrically necessary dislocations on slip systems: application to single and multi-crystals of ice. Modelling and Simulation in Materials Science and Engineering 25, 025010(27pp).

Richeton, T., Wang, G. F., Fressengeas, C., 2011. Continuity constraints at the interfaces and their consequences on the work hardening of metal-matrix composites. Journal of the Mechanics and Physics of Solids 59, 2023–2043.

Rollett, A. D., Lebensohn, R. A., Groeber, M., Choi, Y., J., L., Rohrer, G. S., 2010. Stress hot spots in viscoplastic deformation of polycrystals. Modell. Simul. Mater. Sci. Eng. 18, 074005.

Rovinelli, A., Guilhem, Y., Proudhon, H., Lebensohn, R. A., Ludwig, W., Sangid, M. D., 2017. Assessing reliability of fatigue indicator parameters for small crack growth via a probabilistic framework. Modell. Simul. Mater. Sci. Eng. 25, 045010.

Rovinelli, A., Sangid, M. D., Proudhon, H., Guilhem, Y., Lebensohn, R. A., Ludwig, W., 2018. Predicting the 3-D fatigue crack growth rate of short cracks using multimodal data via Bayesian network: in-situ experiments and crystal plasticity simulations. Journal of the Mechanics and Physics of Solids 115, 208–229.

Roy, A., Acharya, A., 2005. Finite element approximation of field dislocation mechanics. J. Mech. Phys. Solids 53, 143–170.

Roy, A., Acharya, A., 2006. Size effects and idealized dislocation microstructure at small scales : Predictions of a Phenomenological model of Mesoscopic Field Dislocation Mechanics : Part II. Journal of the Mechanics and Physics of Solids 54, 1711–1743.

Roy, A., Puri, S., Acharya, A., 2007. Phenomenological mesoscopic field dislocation mechanics, lower-order gradient plasticity, and transport of mean excess dislocation density. Model. Simul. Mater. Sci. Eng. 15, 167–180.

Sabar, H., Berveiller, M., Favier, V., Berbenni, S., 2002. A new class of micro-macro models for elastic-viscoplastic heterogeneous materials. International Journal of Solids and Structures 39, 3257–3276.

Scheriau, S., Pippan, R., 2008. Influence of grain size on orientation changes during plastic deformation. Materials Science and Engineering A 493, 48–52.

Schwarz, K. W., 1999. Simulation of dislocations on the mesoscopic scale I. Methods and examples. Journal of Applied Physics 85 (1), 108–119.

Shanthraj, P., Eisenlohr, P., Diehl, M., Roters, F., 2015. Numerically robust spectral methods for crystal plasticity simulations of heterogeneous materials. International Journal of Plasticity 66, 31–45.

Sharma, L., Peerlings, R. H. J., Shanthraj, P., , Roters, F., Geers, M. G. D., 2012.

FFT-based interface decohesion modelling by a nonlocal interphase. Adv. Model. Simul. Eng. Sci. 5, 7.

Smyshlyaev, V. P., Fleck, N. A., 1996. The role of strain gradients in the grain size effect for polycrystals. Journal of the Mechanics and Physics of Solids 44, 465–495.

Suquet, P., Moulinec, H., Castelnau, O., Montagnat, M., Lahellec, N., Grennerat, F., Duval, P., Brenner, R., 2012. Multi-scale modeling of the mechanical behavior of polycrystalline ice under transient creep. Procedia IUTAM 3, 76–90.

Taupin, V., Berbenni, S., Fressengeas, C., 2012. Size effects on the hardening of channel-type microstructures: a field dislocation mechanics-based approach. Acta Materialia 60, 664–673.

Taupin, V., Berbenni, S., Fressengeas, C., Bouaziz, O., 2010. On particle size effects: An internal length mean field approach using field dislocation mechanics. Acta Materialia 58, 5532–5544.

Taupin, V., Varadhan, S., Chevy, J., Fressengeas, C., Beaudoin, A. J., Montagnat, M., Duval, P., 2007. Effects of size on the dynamics of dislocations in ice single crystals. Physical Review Letters 99, 155507.

Thompson, A., Baskes, M. I., Flanagan, W. F., 1973. The dependence of polycrystal work hardening on grain size. Acta Metallurgica 21, 1017–1028.

Upadhyay, M. V., Capolungo, L., Taupin, V., Fressengeas, C., Lebensohn, R. A., 2016. A higher order elasto-viscoplastic model using fast fourier transforms: Effects of lattice curvatures on mechanical response of nanocrystalline metals. Int. J. Plast. 83, 126–152.

Van der Giessen, E., Needleman, A., 1995. Discrete dislocation plasticity: A simple planar approach. Modelling and Simulation in Materials Science and Engineering 3, 689–735.

Varadhan, S., Baudoin, A. J., Acharya, A., Fressengeas, C., 2006. Dislocation transport using Galerkin/least squares formulation. Modelling and Simulation in Ma-

terials Science and Engineering 14, 1245–1270.

Varadhan, S., Beaudoin, A. J., Fressengeas, C., 2009. Lattice incompatibility and strain-aging in single crystals. Journal of the Mechanics and Physics of Solids 57, 1733–1748.

Verdier, M., Fivel, M., Groma, I., 1998. Mesoscopic scale simulation of dislocation dynamics in FCC metals: Principles and applications. Modelling and Simulation in Materials Science Engineering 6, 755–770.

Vidyasagar, A., Tutcuoglu, A. D., Kochmann, D. M., 2018. Deformation patterning in finite-strain crystal plasticity by spectral homogenization with application to magnesium. Comp. Meth. Appl. Mech. Eng. 335, 584–609.

Vinogradov, V., Milton, G. W., 2008. An accelerated FFT algorithm for thermoelastic and non-linear composites. Int. J. Num. Meth. Eng. 76, 1678–1695.

Waheed, S., Hao, R., Bhowmik, A., Balint, D. S., Giuliani, F., 2017. A unifying scaling for the Bauschinger effect in highly confined thin films: a discrete dislocation plasticity study. Modelling and Simulation in Materials Science and Engineering 25 (5), 054003.

Wallis, D., Hansen, L. N., Britton, T. B., Wilkinson, A. J., 2016. Geometrically necessary dislocation densities in olivine obtained using high-angular resolution electron backscatter diffraction. Ultramicroscopy 168, 34–45.

Wang, H., Wu, P. D., Tomé, C. N., Huang, Y., 2010. A finite strain elastic-viscoplastic self-consistent model for polycrystalline materials. Journal of the Mechanics and Physics of Solids 58, 594–612.

Weng, G. J., 1983. A micromechanical theory of grain size dependence in metal plasticity. Journal of the Mechanics and Physics of Solids 31, 193–203.

Willot, F., 2015. Fourier-based schemes for computing the mechanical response of composites with accurate local fields. Comptes Rendus Mecanique 343, 232–245.

Willot, F., Pellegrini, Y. P., 2008. Fast Fourier transform computations and build-up

of plastic deformation in 2D, elastic-perfectly plastic, pixelwise disordered porous media. Continuum Models and Discrete Systems, D. Jeulin and S. Forest (eds.), CMDS11, Ecole des Mines Paris, 443–449.

Wulfinghoff, S., Forest, S., Böhlke, T., 2015. Strain gradient plasticity modeling of cyclic behavior of laminate structures. Journal of the Mechanics and Physics of Solids 79, 1–20.

Zeghadi, A., Forest, S., Gourgues, A. F., Bouaziz, O., 2005. Cosserat continuum modelling of grain size effects in metal polycrystals. Proceedings in Applied Mathematics and Mechanics (PAMM) 5, 79–82.